A phase-field model for ferroelectric materials—Based on the multiphase-field method

Ling Fan [a,*], Martin Reder [a,c], Daniel Schneider [a,b,c], Manuel Hinterstein [a,d], Britta Nestler [a,b,c]

[a] Institute for Applied Materials (IAM), Karlsruhe Institute of Technology, 76131, Karlsruhe, Germany
[b] Institute of Nanotechnology (INT), Karlsruhe Institute of Technology, 76131, Karlsruhe, Germany
[c] Institute of Digital Materials Science, Karlsruhe University of Applied Sciences, 76133, Karlsruhe, Germany
[d] Fraunhofer Institute for Mechanics of Materials, 79108, Freiburg, Germany

Keywords:
Multiphase-field method
Ferroelectric material
Domain structure

A B S T R A C T

A novel phase-field model is developed to investigate the domain structure in ferroelectric materials subjected to an external field. Differing from the time-dependent Ginzburg–Landau (TDGL) theory that describes domain structures based on the spatial and temporal evolution of polarization, our model utilizes the multiphase-field approach to calculate domain structures by minimizing the total energy functional with respect to the multiphase-field order parameter $\boldsymbol{\phi}$. The energy functional in the proposed model comprises the general multiphase interfacial energy and the phase-dependent bulk energy, accounting for the contributions from domain walls, and mechanical as well as electric fields. By considering the interplay between the different energy components, the model provides insights into the complex domain structure of ferroelectric materials and their response to external stimuli. This comprehensive approach is validated through simulations of both single-crystal and polycrystalline structures. The approach presented in this study simplifies the computational coefficients required to analyze the domain structure in ferroelectric materials, compared to the TDGL approach, by disregarding the Landau potential. This makes it possible to analyze the domain structure of materials without Landau coefficients. Furthermore, the proposed model serves as a reference for applying the multiphase-field concept to ferroelectric materials.

1. Introduction

The phase-field method is a highly effective mesoscale computational approach used to model and predict the spatial and temporal evolution of material microstructures, along with their corresponding responses and properties under external stimuli. The phase-field approach was initially introduced for solidification [1–4] and has been widely applied to various phenomena until now. This includes solid-state phase transformations [5–8], particle coarsening [9–11], multiphase flow [12–14], mechanical deformation [15–19], etc. In the context of time-dependent Ginzburg–Landau (TDGL) theories, the phase-field method has also been successfully employed to predict the domain structure and the phase transformation for ferroelectric materials [20–26]. The research on ferroelectric materials, using the phase-field method, has extended to various types of materials, including single crystal/polycrystal bulk materials [24,27–29], epitaxial thin-film materials [25], ferroelectric semiconductor materials [30–32], superlattices [33,34], and ferroelectric nanostructures, such as nano islands [35], nanodots as well as nanowires [36,37]. The multiphase-field model, which is an extension of the phase-field method to account for any number of phases and components, has been the subject of extensive study and development within the research community (see, e.g., Refs. [4,38–41]). Recently, there has been a growing interest in using the multiphase-field method to analyze ferroelectric materials [42–49].

Thus, Torres et al. developed a multiphase-field model to explain the mechanisms responsible for the coexisting ferroelectric phases and enhanced electromechanical properties found in experiments performed near the polymorphic phase boundary (PPB) in barium zirconate titanate-barium calcium titanate (BZT-BCT) [42–45]. Their model couples four Allen–Cahn equations to study the domain structures and transformation kinetics for the coexisting ferroelectric phases. The homogeneous free energy density of the individual ferroelectric phases is taken into account with phase-dependent Landau coefficients, allowing a thermodynamically correct and more accurate analysis near the interferroelectric phase transitions. However, the model neglects the mechanical field that directs the formation of the ferroelastic domain wall (non-180° domain wall), and the simple coupling of the

* Corresponding author.
E-mail addresses: ling.fan@kit.edu (L. Fan), daniel.schneider@kit.edu (D. Schneider), manuel.hinterstein@kit.edu (M. Hinterstein).

Allen–Cahn equations limits the calculations to a single crystal in one or two spatial dimensions [43]. Fanet al. [46] also proposed a phase-field model for polycrystal ferroelectric materials with multiple ferroelectric phases. Instead of combining the Allen–Cahn equations, their model combined the TDGL theory with the general multiphase-field functional [40], together with a model for the thermodynamically consistent mapping of mechanical balance conditions at grain and phase boundaries [50–52]. This extends the numerical calculations to polycrystalline ferroelectrics with multiple ferroelectric phases in arbitrary dimensions and allows the accurate description as well as the quantitative analysis of the influence of the mechanical field on the domain structure. Relying on the new model, they investigated the phase transformation between ferroelectric tetragonal and ferroelectric rhombohedral phases and the corresponding domain structures with or without the external stimuli in the polycrystal PIC 151 material.

Additionally, the multiphase-field method has found application outside of perovskite ferroelectric materials, as recent studies have shown. For example, Sugathan et al. [53] used the multiphase-field approach proposed by Steinbach et al. [54] to develop a model for simulating the switching behavior of polycrystalline $Hf_{1-x}Zr_xO_2$ thin films. Other researchers, such as Zhu et al. [55] and Li et al. [56], and more recently, Chen et al. [47] and Li et al. [48], have also employed the multiphase-field method to study the domain structures in Hf-based ferroelectric materials.

Although the primary motivation of these works [42–48] is to distinguish different ferroelectric phases or paraelectric/ferroelectric phases, the evolution of polarization is still described by the TDGL model. In the context of the TDGL model, the polarization vector serves as the order parameter. The model effectively captures the interface properties through a comprehensive six-order Landau potential, alongside the domain wall gradient energy [27]. Consequently, the accurate characterization of domain walls necessitates the availability of Landau coefficients and gradient coefficients. Nevertheless, the experimental determination or theoretical calculation of these parameters poses significant challenges in the field of materials science. As of the present time, the number of materials with available Landau potentials is notably limited and includes $BaTiO_3$, $PbTiO_3$, $PbZr_{1-x}Ti_xO_3$, $BiFeO_3$, $CaTiO_3$, $SrTiO_3$, $KNa_{1-x}Nb_xO_3$, $LiNbO_3$, $LiTaO_3$, $SrBi_2Nb_2O_9$, and $Sr_{0.8}Bi_{2.2}Ta_2O_9$ [57]. However, the ferroelectrics discovered go far beyond these. In light of the mentioned constraints, a comprehensive investigation of domain structures in materials lacking the required coefficients, such as the aforementioned Hf-based ferroelectric materials that are not perovskites, is impeded. Interestingly, Guin et al. [49] proposed a new approach based on the multiphase-field approach to describe the nonlinear domain dynamics, by treating the possible polarization state as the phase-field order parameter, instead of using polarization directly. They suggest that the formation of the domain structure depends on the phase transformation between different states of the order parameter. Building on this idea, we have developed a novel phase-field model in our current work to investigate the domain structures and material properties of ferroelectric materials.

The multiphase-field approach is based on the method proposed by Nestler et al. [40] and the mechanical solution is performed using the jump condition technique described in the Refs. [50–52]. In contrast to Ref. [49], our study uses a multi-obstacle potential in conjunction with a distinct gradient energy formulation to characterize the interfacial energy and thereby capture the domain wall properties. Furthermore, the multiphase and multicomponent approach [40] enables the simulation of both single crystal and polycrystalline structures that include different ferroelectric phases. Importantly, compared to the lack of a mechanical field analysis in Ref. [49], the use of the jump condition methodology enables a straightforward calculation of the mechanical field across grain boundaries, ferroelectric phase interfaces, and domain walls. In particular, by replacing the Landau potential with a multi-obstacle potential and the domain wall energy density with a phase-field gradient energy density, the new model enables the numerical simulation of ferroelectric materials with insufficient Landau coefficients and gradient coefficients. Moreover, in the proposed approach, the interfacial energy parameter used to capture the interfacial properties within the multiphase framework could be independently and physically tailored for each interface. It can denote the interfacial energy between different domain variants or between grains with different orientations, or even cross interfaces separating distinct ferroelectric phases. The paper begins with a presentation of the novel model, followed by computational analyses of the domain structures in both single-crystal and polycrystalline systems with/without the application of an external field. In addition, the properties of the polarization hysteresis and the strain hysteresis loop are calculated.

2. Methodology

2.1. Multiphase-field energy model of polycrystalline ferroelectric materials

The polycrystalline ferroelectric materials comprise grains with different orientations, each of which may contain a single ferroelectric phase with distinct polarization variants (such as the tetragonal phase in $BaTiO_3$), or multiple ferroelectric phases with different domain variants (such as the coexisting tetragonal and rhombohedral phases in Pb(Ti, Zr)O_3), as shown in Figs. 1(a)–(b). Accordingly, the study proposes a method to define the polarization variants in each ferroelectric phase with identical amplitude but different polar orientations as "phases (ϕ_α)". The formation of the domain structure in the ferroelectric material depends on the transformation between these phases, as shown in Fig. 1(c). The number of polarization variants, also referred to as physical region (ϕ_α) in this work, is determined by the crystal structure of the ferroelectric material. The ferroelectric tetragonal phase, for example, has six polarization variants oriented along the < 100>-directions, which can form both in-plane and out-of-plane 180° or 90° domain walls, as shown in Figs. 1(c) and (d).

Based on the general multiphase-field approach formulated by Nestler et al. [40], together with a model for the thermodynamically consistent mapping of mechanical balance conditions at the grain and phase boundaries [50–52], the total energy functional of the novel model describing the above concept can thus be expressed as:

$$\mathcal{F} = \int_V \Big[f_{\text{grad}}(\nabla\boldsymbol{\phi}) + \frac{1}{\epsilon}\omega_{\text{ob}}(\boldsymbol{\phi}) + \sum_{\alpha=1}^{N} \big(f^{\alpha}_{\text{elast}}(\boldsymbol{\varepsilon}^{\alpha}, \boldsymbol{P}^{\alpha}) + f^{\alpha}_{\text{elec}}(\boldsymbol{P}^{\alpha}, \boldsymbol{E}_{\text{ext}}) \big) h^{\alpha}(\boldsymbol{\phi}) \Big] \, \mathrm{d}V. \tag{1}$$

Here, $\boldsymbol{\phi}$ is the order parameter of the phase field that symbolizes distinct physical regions such as domain variants, ferroelectric phases, or grains. The variable N quantifies the total number of these regions delineated by the diffuse interface. For a single crystal with a ferroelectric phase, for example, N represents the number of polarization variants of the ferroelectric phase. Such an interface refers to a domain wall and the single region corresponds to a single domain, i.e., a ferroelectric polarization variant. In this case, as shown in Fig. 1(c), the order parameter thus is $\phi_\alpha(\boldsymbol{x}, t) = 1$ within the single domain α, while outside of α, it is $\phi_\alpha(\boldsymbol{x}, t) = 0$. In the domain wall region, $\phi_\alpha(\boldsymbol{x}, t)$ smoothly changes from 0 to 1. In a polycrystalline system comprising a single ferroelectric phase (Fig. 1(a)), the diffuse interface can also be the grain boundary and the additional $\boldsymbol{\phi}_{\text{grain}} = \sum_{\alpha=1}^{K} \phi_\alpha$ is introduced to describe grains with varying orientations. Here, K denotes the number of polarization variants in the ferroelectric phase, resulting in $N = MK$, where M is the grain count. For the polycrystalline system, which consists of ferroelectric phases (Fig. 1(b)), the interface can also represent the interphase boundaries separating domains of different phases. In this scenario, each grain is defined as $\boldsymbol{\phi}_{\text{grain}} = \sum_{\text{FP}=1}^{L} \sum_{\alpha=1}^{K} \phi_{\text{FP},\alpha}(\boldsymbol{x}, t)$, with $\sum_{\alpha=1}^{K} \phi_{\text{FP},\alpha}(\boldsymbol{x}, t)$, the polarization variants in each ferroelectric phase. FP denotes the ferroelectric phase and L signifies the total number of these phases. Hence the total number of polarization variants across all grains is given by $N = M \sum_{\text{FP}=1}^{L} K_{FP}$, where K_{FP} corresponds to the count of

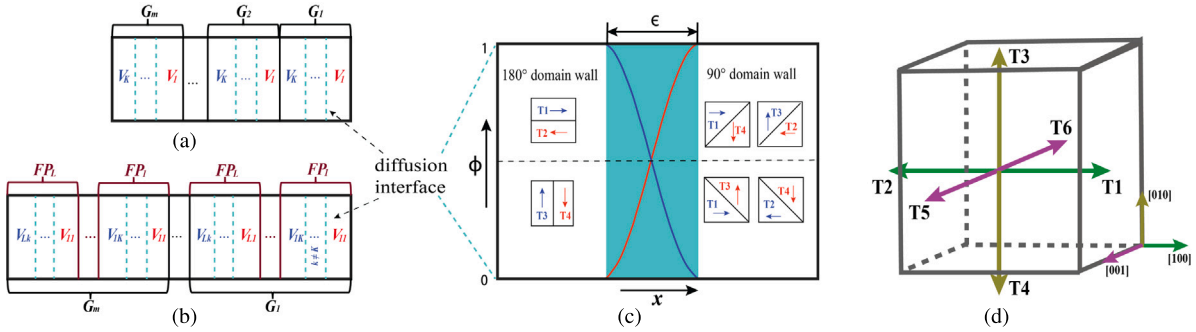

Fig. 1. The scheme used in the current model to calculate domain structures in ferroelectric materials. (a) A polycrystalline structure with a single ferroelectric phase, where $G_m\,(m = 1, 2 \dots m)$ represents the grain m, while the kth variant of the ferroelectric phase is denoted by $V_k\,(k = 1, 2 \dots k)$; (b) A polycrystalline structure with multiple ferroelectric phases, in which FP_1 to FP_L represent the ferroelectric phase from 1 to L; (c) A description of the in-plane ferroelectric tetragonal variants over the diffusion region, where ϵ relates to the interfacial thickness. (d) The in-plane (T1–T4) and out-of-plane (T5 and T6) polarization variants in the tetragonal phase.

polarization variants in the ferroelectric phase FP. In addition, the local constraint $\sum_{\alpha}^{N} \phi_\alpha(\boldsymbol{x}, t) = 1$ is always fulfilled, regardless of whether the system under consideration is a monocrystalline or a polycrystalline structure.

In Eq. (1), the interfacial energy density between polarization variants, phases, or grains is given by the first two terms on the right-hand side, where $f_{\text{grad}}(\nabla\boldsymbol{\phi})$ denotes the gradient energy density and $\frac{1}{\epsilon}\omega_{\text{ob}}(\boldsymbol{\phi})$ is the multi-obstacle-type potential energy density, with ϵ scaling the interface thickness, which in this case is given by $\pi^2/4\,\epsilon$. Apart from this, the summation part in Eq. (1) represents the phase-dependent bulk energy consisting of the elastic energy $f^{\alpha}_{\text{elast}}(\boldsymbol{\varepsilon}^{\alpha}, \boldsymbol{P}^{\alpha})$ and the electric energy density $f_{\text{elec}}(\boldsymbol{P}^{\alpha}, \boldsymbol{E}_{\text{ext}})$, in which $\boldsymbol{\varepsilon}^{\alpha}$ denotes the strain tensor and $\boldsymbol{E}_{\text{ext}}$ represents the external electric field. $\boldsymbol{P}^{\alpha}$ is the cross-phase polarization, where the orientation is determined by its material crystal structure, while the amplitude is fixed at the absolute value of the spontaneous polarization. In addition, the use of an interpolation function $h^{\alpha}(\boldsymbol{\phi}) = \phi^{\alpha}$, which satisfies the condition $\sum_{\alpha} h^{\alpha}(\boldsymbol{\phi}) = 1$, allows us to capture the transformation of the polarization state across the interface, which facilitates the calculation of the bulk energy in the diffusion region. Different choices for the interpolation functions are also applicable. An overview and a deeper discussion can be found in [58].

Based on Ref. [54], the gradient energy density in Eq. (1) can be formulated as:

$$f_{\text{grad}}(\nabla\boldsymbol{\phi}) = \epsilon \sum_{\alpha,\beta>\alpha} \gamma^{\alpha\beta} \nabla\phi_\alpha \nabla\phi_\beta, \tag{2}$$

by using $\gamma^{\alpha\beta}$ as the isotropic interfacial energy density. The adoption of a multi-obstacle potential allows the phase-field variables to attain values of 0 and 1 within the intended interface width. This property facilitates the storage of interface information and conserves memory in numerical computations [41]. Furthermore, the double obstacle potential effectively prevents the expansion of multiple junctions into the interface region [41]. Hence the multi-obstacle potential is considered in this work, which can be expressed as:

$$\frac{1}{\epsilon}\omega_{\text{ob}}(\boldsymbol{\phi}) = \frac{16}{\epsilon\pi^2} \sum_{\alpha<\beta}^{N,N} \gamma^{\alpha\beta}\phi^{\alpha}\phi^{\beta} \tag{3}$$

In the event that the $N-$tuple $\boldsymbol{\phi}$ does not reside on the Gibbs simplex $\mathcal{G} = \{\boldsymbol{\phi} | \sum_{\alpha}\phi_\alpha = 1, \text{and}\, \phi_\alpha \geq 0\}$, the value of $\omega_{\text{ob}}(\boldsymbol{\phi})$ is assigned to infinity. We note that a multiwell potential can also be considered, although this is not the focus of the current study.

The polarization orientation automatically rotates with the grain orientation, as the polarization is interpolated based on the phase-field order parameter $\boldsymbol{\phi}$. As a result, the elastic energy density for each phase in the polycrystalline ferroelectric material is defined as follows:

$$f^{\alpha}_{\text{elast}}(\boldsymbol{\varepsilon}^{\alpha}, \boldsymbol{P}^{\alpha}) = \frac{1}{2}\left[[\boldsymbol{\varepsilon}^{\alpha} - \tilde{\boldsymbol{\varepsilon}}^{\alpha}(\boldsymbol{P}^{\alpha})] \cdot \boldsymbol{C}^{\alpha} \cdot [\boldsymbol{\varepsilon}^{\alpha} - \tilde{\boldsymbol{\varepsilon}}^{\alpha}(\boldsymbol{P}^{\alpha})]\right]. \tag{4}$$

$\boldsymbol{C}^{\alpha}$ denotes the elastic stiffness of the material, which is dependent on the ferroelectric phase, but independent of the variant. The symbols $\boldsymbol{\varepsilon}^{\alpha}$ and $\tilde{\boldsymbol{\varepsilon}}^{\alpha}(\boldsymbol{P}^{\alpha})$ respectively represent the total strain and the inelastic strain. Using the Einstein summation convention, $\tilde{\varepsilon}^{\alpha}_{ij}(\boldsymbol{P}^{\alpha})$ is defined as:

$$\tilde{\varepsilon}^{\alpha}_{ij}(\boldsymbol{P}^{\alpha}) = Q_{ijkl} P^{\alpha}_{k} P^{\alpha}_{l}, \tag{5}$$

in which $\boldsymbol{Q}^{\alpha}$ is the ferroelectric phase-dependent electrostrictive coefficient. The total strain resulting from the gradient of the displacement $\boldsymbol{u}$ is defined as:

$$\boldsymbol{\varepsilon} = \frac{1}{2}\left[\nabla\boldsymbol{u} + (\nabla\boldsymbol{u})^{\text{T}}\right]. \tag{6}$$

$\boldsymbol{\varepsilon}$ can be decomposed into phase components, using $\boldsymbol{\varepsilon} = \sum_{\alpha}\boldsymbol{\varepsilon}^{\alpha}h^{\alpha}(\boldsymbol{\phi})$, as explained in Refs. [50–52,59,60]. Similarly, $\boldsymbol{\sigma}$ follows a similar volumetric decomposition approach. As mentioned earlier, we apply the jump condition approach to deal with the mechanical field. This method uses normal stress components and tangential strain components to define a consistent potential type, which in turn helps in formulating the driving force. Further details can be found in Appendix A.

When an external electric field $\boldsymbol{E}_{\text{ext}}$ is present, the electrostatic energy $f^{\alpha}_{\text{elec}}(\boldsymbol{P}^{\alpha})$ in polycrystalline ferroelectric materials results from both the energy density of the long-range multiple dipole–dipole electric interactions and the external electric energy. This energy density can be obtained by:

$$f_{\text{elec}}(\boldsymbol{P}^{\alpha}) = -\frac{1}{2}\nabla\psi \cdot \boldsymbol{P}^{\alpha} - \boldsymbol{E}_{\text{ext}}\boldsymbol{P}^{\alpha}. \tag{7}$$

ψ is the electrostatic potential for the long-range dipoles and $\nabla\psi$ represents the depolarization electric field in the global coordinate. Depending on the electrostatic equilibrium equation of the electric displacement $D_{i,i} = 0$, with $D_i = \kappa_0\kappa_r\nabla\psi + P_i$, ψ can be solved by:

$$\kappa_0\kappa_r\Delta\psi = \nabla \cdot \boldsymbol{P}^{\alpha}. \tag{8}$$

$\kappa_0 = 8.85 \times 10^{-12}$ F/m denotes the absolute dielectric permittivity, while $\kappa_r = 50$ is known as the background dielectric permittivity.

2.2. Governing equation

Based on the work of Refs. [6,41,54], the minimization of the energy functional Eq. (1) leads to the computation of the domain structure, performed according to the order parameter ϕ_α:

$$\frac{\partial\phi_\alpha(\boldsymbol{x}, t)}{\partial t} = -\frac{1}{\widetilde{N}\epsilon}\sum_{\beta\neq\alpha}^{\widetilde{N}}\left[M^{\alpha\beta}\left(\frac{\delta\mathcal{F}}{\delta\phi_\alpha} + \epsilon\hat{\alpha}(\phi_\alpha, \nabla\phi_\alpha)\right.\right. \\ \left.\left. - \frac{\delta\mathcal{F}}{\delta\phi_\beta} - \epsilon\hat{\alpha}(\phi_\beta, \nabla\phi_\beta)\right)\right] + \frac{\partial\mathcal{L}}{\partial\phi_\alpha}, \tag{9}$$

where $M^{\alpha\beta}$ is known as the phase-field mobility for the phases α and β, and N denotes the number of the locally active phases. $\delta\mathcal{F}/\delta\phi_\alpha$ is the variational derivative of the total energy, with respect to ϕ_α, defined by

$$\frac{\delta\mathcal{F}}{\delta\phi_\alpha} = \frac{\partial f}{\partial\phi_\alpha} - \nabla\cdot\frac{\partial f}{\partial\nabla\phi_\alpha} \tag{10}$$

According to Ref. [6,16,52], the resulting bulk driving force arising from the elastic energy density with the jump condition approach can be characterized as:

$$\boldsymbol{\Delta}^{\alpha\beta}_{\text{elast}}(\boldsymbol{\phi},\boldsymbol{\varepsilon},\boldsymbol{P}) = \frac{\partial W}{\partial\phi_\beta} - \frac{\partial W}{\partial\phi_\alpha}, \tag{11}$$

where W is the overall elastic potential based on continuous variables. The detailed expression can be found in Appendix A.

The driving force resulting from the electrostatic energy can be written as:

$$\boldsymbol{\Delta}^{\alpha\beta}_{\text{elec}}(\boldsymbol{P},\boldsymbol{E}) = f^{\beta}_{\text{elec}}\frac{\partial h^{\beta}(\boldsymbol{\phi})}{\partial\phi_\beta} - f^{\alpha}_{\text{elec}}\frac{\partial h^{\alpha}(\boldsymbol{\phi})}{\partial\phi_\alpha}. \tag{12}$$

To describe the polarization variations that can form at the interface characterized by potential energy with multiple obstacles, including domain boundaries, phase boundaries, or grain boundaries, as shown in Eq. (1), we introduce a noise term $\pounds$ to account for the thermal fluctuations described as follows:

$$\pounds = \sum_{\alpha<\beta<\delta}^{N,N,N}\phi_\alpha\phi_\beta\phi_\delta\cdot D\cdot A. \tag{13}$$

The variable D characterizes the type of noise distribution, which can take various forms, such as uniform, Gaussian, and others, while A determines the magnitude of the fluctuations. It should be noted that the inclusion of the noise term $\pounds$ to model the nucleation of polarization variations is not essential if the simulation includes a multiwell potential. This is attributed to the isotropic of the interface in the multiwell potential, which induces thermodynamic fluctuations that occur naturally at the interface, in the presence of external stimuli. To ensure both a reasonable interface quality and highly effective simulation efficiency, an isotropic gradient energy density

$$\epsilon\hat{\alpha}(\phi_\alpha,\nabla\phi_\alpha) = \epsilon\gamma^{c}_{\alpha}\left(\Delta\phi_\alpha - |\nabla\phi_\alpha|\nabla\cdot\left(\frac{\nabla\phi_\alpha}{|\nabla\phi_\alpha|}\right)\right) \tag{14}$$

is integrated into the multiphase content and included in the phase-field evolution Eq. (9). This helps to strike a balance between low interfacial energy, high bulk driving forces, and an appropriate grid resolution. Note that the second term in Eq. (14) compensates for the curvature-minimizing property of the Laplace operator, thus preserving the equilibrium profile of the phase field, while preventing changes in its shape [6,61]. Regarding the nucleation mechanism of Eq. (13) and the physical meaning behind Eq. (14), the reader is recommended to Ref. [6].

The mechanical equilibrium can be expressed by the static momentum balance equation:

$$\nabla\cdot\boldsymbol{\sigma} = 0, \tag{15}$$

in which $\boldsymbol{\sigma}$ represents the elastic stress that is solved based on a mechanical jump condition approach [50,52].

2.3. Numerical simulations

To validate the new multiphase-field model in the ferroelectric material, we performed simulations using our in-house software package, Pace3D (Parallel Algorithms for Crystal Evolution in 3D) [62]. Specifically, we used a finite difference algorithm with an explicit forward Euler scheme to solve the phase-field evolution equation (Eq. (9)) and determine the domain structure at room temperature (T = 300 K). After solving the phase-field evolution equation (Eq. (9)), we have implicitly solved the mechanical equilibrium condition (Eq. (15)) in every time step. For details on this procedure, we refer the reader to Refs. [15,17,50]. Additionally, we solved the electrostatic equilibrium condition (Eq. (8)) using the conjugate gradient approach. To reduce simulation time, the domain was decomposed in both x- and y-directions using the message passing interface (MPI) standard. The computational structures for both monocrystalline and polycrystalline systems were created using the Voronoi tessellation. The domain was discretized into cells with uniform dimensions of $\Delta x = \Delta y = \Delta z = 0.5$ nm, regardless of the system size.

Table 1
The phase-field parameters and material coefficients used in the current simulation.

Material coefficients	Symbol	Value	Unit
Dielectric stiffness	α_1	(T-381)*3.34[a]	$10^5\cdot$[m/F]
Interfacial length parameter	$\epsilon/\Delta x$	4	–
Interfacial energy	$\gamma_{\alpha\beta}$	0.01	J/m^2
Phase-field mobility	$M^{\alpha\beta}$	1	–
Elastic tensor $\boldsymbol{C}$	C_{11}	27.50	$10^{10}\cdot$[N/m^2]
	C_{12}	17.90	$10^{10}\cdot$[N/m^2]
	C_{44}	4.80	$10^{10}\cdot$[N/m^2]
Electrostrictive tensor $\boldsymbol{Q}$	Q_{11}	11.00	$10^{-2}\cdot$[m^4/C^2]
	Q_{12}	4.50	$10^{-2}\cdot$[m^4/C^2]
	Q_{44}	7.75	$10^{-2}\cdot$[m^4/C^2]
Gradient coefficient	G_{11}	51	$10^{-11}\cdot$[Nm^4/C^{-2}]

[a] Values of $\alpha_1, \boldsymbol{C}$ and $\boldsymbol{Q}$ are taken from Ref. [31]

$BaTiO_3$ (BTO) was selected as the model material for this investigation, and the simulation was limited to one ferroelectric phase, namely the tetragonal phase. To ensure numerical stability, we set the diffuse interface width parameter ϵ to $4\Delta x$, resulting in an interface width of about $6.5\Delta x = 3.25$ nm, since a multi-obstacle-type potential is used. As outlined in Ref. [63], the thickness of the 90° domain wall in BTO spans from 2 nm to 25 nm. Therefore, it could be concluded that the interface width in the simulation also has a physical significance. To convey a physical implication and not just a numerical value, we set the interfacial energy $\gamma^{\alpha\beta}$ for each variant to the 180° domain wall energy in 1 nm, which can be written as:

$$\gamma^{\alpha\beta} = 1.26|\alpha_1|l_0P_0^2, \tag{16}$$

based on Ref. [27]. α_1 is the dielectric stiffness at room temperature. l_0 is defined as $\sqrt{G_{11}/(0.6|\alpha_1|)}$, where G_{11} represents the gradient coefficient. Additionally, $P_0 = 26\,\mu$C/cm^2 [64] is the spontaneous polarization. The mobility coefficient $M^{\alpha\beta}$ of the tetragonal variants, which also represents the domain wall mobility in the current model, was set to one. At room temperature, the grains are immobilized in the BTO material, so we fixed the grain boundaries in our simulations by setting the grain interfacial mobility $M^{\alpha\beta}$ to zero. The elastic stiffness tensors were treated as isotropic and taken from Ref. [31]. To increase accuracy, the input data is transformed into a dimensionless form. The corresponding transformation method is explained in more detail in Appendix B. For clarity, we listed the simulated parameters in Table 1.

3. Simulation results and discussion

3.1. Phase-field simulation in the single-crystal structure

3.1.1. Formulation of a ferroelectric domain structure

At the beginning of the numerical modeling, the domain structure of the tetragonal phase within a single grain was calculated in the absence of an external field. For computational convenience, quasi-2D simulations (see Fig. 2) are performed on a $100\times100\times1$ cell in the following subsections to illustrate the formation of the domain structure and its response to an external field. To validate the dimensional extension of

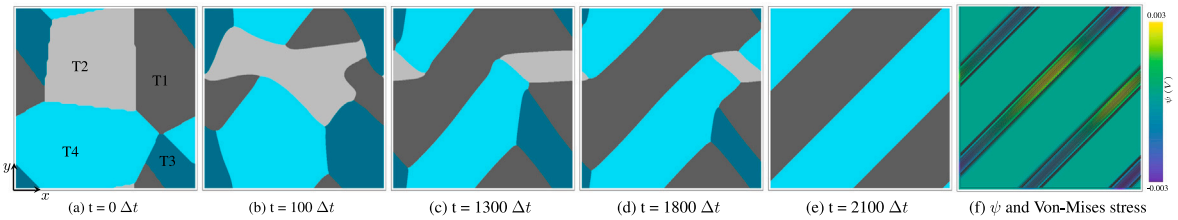

Fig. 2. The initial configuration (a) and temporal evolution (b–e) of the 2D single crystal in the simulation. (f) illustrates the distribution of the electric potential ψ and the von Mises stress (black lines) at 2100Δt. The orientation of the polarization for each respective variant can be seen in Fig. 1(d).

the model, we also performed a 3D calculation of a single crystal with $100 \times 100 \times 100$ voxels (see Fig. 3). Periodic boundary conditions are employed for all fields. Fig. 2(a) shows the initialization of the quasi-2D simulation, where four tetragonal polarization variants randomly occupy the computational area of a single grain. The corresponding polarization orientation of each tetragonal variant is shown in Fig. 1(d). The dark color in Fig. 2 represents the variant whose polarization direction is aligned with the positive direction of the axis, and vice versa. It should be mentioned that in this case, the governing equation of the phase-field model, Eq. (9), is solved without the nucleation mechanism, since all variants are already present in the initial state. The main transformation of the four polarization states is shown in Figs. 2(b)–(e). To eliminate the effect of the depolarization field, the system can be observed to naturally form a head-to-tail domain structure by consuming T2 and T3 variants, thus avoiding the initially assigned head-to-head or tail-to-tail polarization states. The equilibrium state of the single-grain simulation is demonstrated in Fig. 2(e), in which 90° domain walls form with {110} twin planes, indicating the contribution of the strain energy during the domain formation process. The simulated 90° domain walls of the tetragonal phase with the head-to-tail arrangement are consistent with the calculated result of Wang et al. [24] as well as with our previous work [46], using the conventional TDGL method, providing the first validation of the reliability of our current model. In addition, Fig. 2(f) shows the distribution of ψ, where the black lines on the plot indicate the contours of the von Mises stresses. The uniformity of the electrostatic energy and elastic strains is evident throughout the domain, while variations are observed at the domain walls. It should be noted that in addition to the lamellar polarization configuration, more complex but reasonable domain structures can also be obtained with the current simulation parameters, depending on the original setup or the computed geometry. The equilibrium domain structure of a 500×500 grain, for instance, can be found in Appendix C (Fig. 13).

The initial state and the simulated results of the 3D single crystal are shown in the first row of Fig. 3. Again, the polarization configuration of each variant refers to Fig. 1(d). The dark-colored regions represent the tetragonal variants with the polarization direction aligned along with the positive x, y, or z-axis, while the corresponding light-colored regions represent the variants with polarization in the opposite direction. The computed result shows the head-to-tail 90° domain wall, constructed by the tetragonal variants T2 and T6. The total strains ϵ_{11} and ϵ_{33} at equilibrium are also shown in the first row of Fig. 3. The domain structure and the distribution of the total strain in the 3D tetragonal single crystal indicate that the formation of the domain structure is also primarily influenced by the strain energy. Fig. 3 also shows the temporal evolution of the morphologies across three sectional planes (xy, xz, and yz), providing insight into the formation mechanism of the domain structure. The sections in the xy, xz, and yz planes are centered at the middle section of the axis perpendicular to the plane and provide a consistent central point for comparison. Simulations from 0 to 100 steps indicate that the depolarization field dismisses the tail-to-tail and head-to-head domain structure. The appearance of the unfilled T6 variant at the boundary in the xz plane is a remarkable observation, suggesting that the formation of the domain structure in one plane is influenced by interactions with other domains. Over time, the 90° domain structure in each plane stabilizes, culminating in the formation of 90° ferroelastic domain structures in the 3D single crystal. One could find that a curved interface emerges during the simulation, exemplified by the curvature domain wall connecting the T4 and T6 variants in the xy-plane at $t = 100\Delta t$, positioned between the highlighted red circles. Notably, such a curved interface may be due to a reduced resolution in the 3D simulation, especially near the triple junction. At the triple junction, the phase interfaces intersect at a 120° angle and advance due to the associated driving force. Consequently, a phase interface bridging two triple junctions can be affected by two directions. Reducing the resolution in the 3D simulation makes significant changes to the phase interface difficult and leads to the manifestation of curvature in the phase interface.

The simulation results demonstrate that the proposed phase-field model is capable of describing the formation of domain structure in ferroelectric materials without an external field. In the following subsection, we provide insight into the behavior of domain switching exposed to an external field.

3.1.2. *Domain switching induced by an electric field*

To further demonstrate the practical applicability of the current model in capturing the behavior of ferroelectric materials, we first simulated polarization switching under an external electric field. The process of such a domain switching can be divided into three main steps: (1) nucleation of a domain with reversed polarization, usually at interfaces or defects due to locally high free energy, (2) fast-forward propagation of domains in the direction of the electric field, due to the high energy of the forward charged domain edge, and (3) lateral domain growth perpendicular to the electric field, enabled by a sidewise motion of the nominal charge-neutral domain wall [65]. In order to model this process in our numerical simulations, the noise $\mathcal{E}$ in Eq. (9) is applied at every fiftieth-time step, with a uniform distribution during the first 1000 iteration steps. Similarly, we enforced periodic boundary conditions on the phase field, the electric field, and the mechanical field to ensure consistency in our simulation.

Fig. 4 shows the simulated results of applying an electric field, $E^*_{\text{ext}} = 1\,(E_{\text{ext}} = E^*_{\text{ext}}|\alpha_1|P_0 \times 10^6\,\text{kV/mm})$, to the equilibrium domain structure depicted in Fig. 2(e), along different tetragonal crystal orientations. Notably, the arrows in (f), (j), (k), and (l) indicate the direction of the induced electric field. To illustrate how the new model can achieve domain switching, we present an example where the simulation of E^*_{ext} is aligned with the T2 direction, as shown in Figs. 4(a)–(f). Initially, the phase-field values of the T2 and T3 variants appear temporarily in small quantities at the binary T1–T4 interface, since noise is applied to the phase field, which can be observed in Fig. 4(a). The energetics of the system determines whether the new phase will grow or not. If the growth of the new phase is energetically favorable, it overcomes the nucleation barrier. However, if it is not favorable, the introduced disturbances disappear within a few time steps. This phenomenon explains why the T2 variant grows, while the T3 variant disappears in Figs. 4(b) and (c). It should be mentioned that this approach enhances the numerical efficiency of the simulation and enables the exact computation of all interpolated quantities. However, the decisive factor is the choice of the interval between two noise

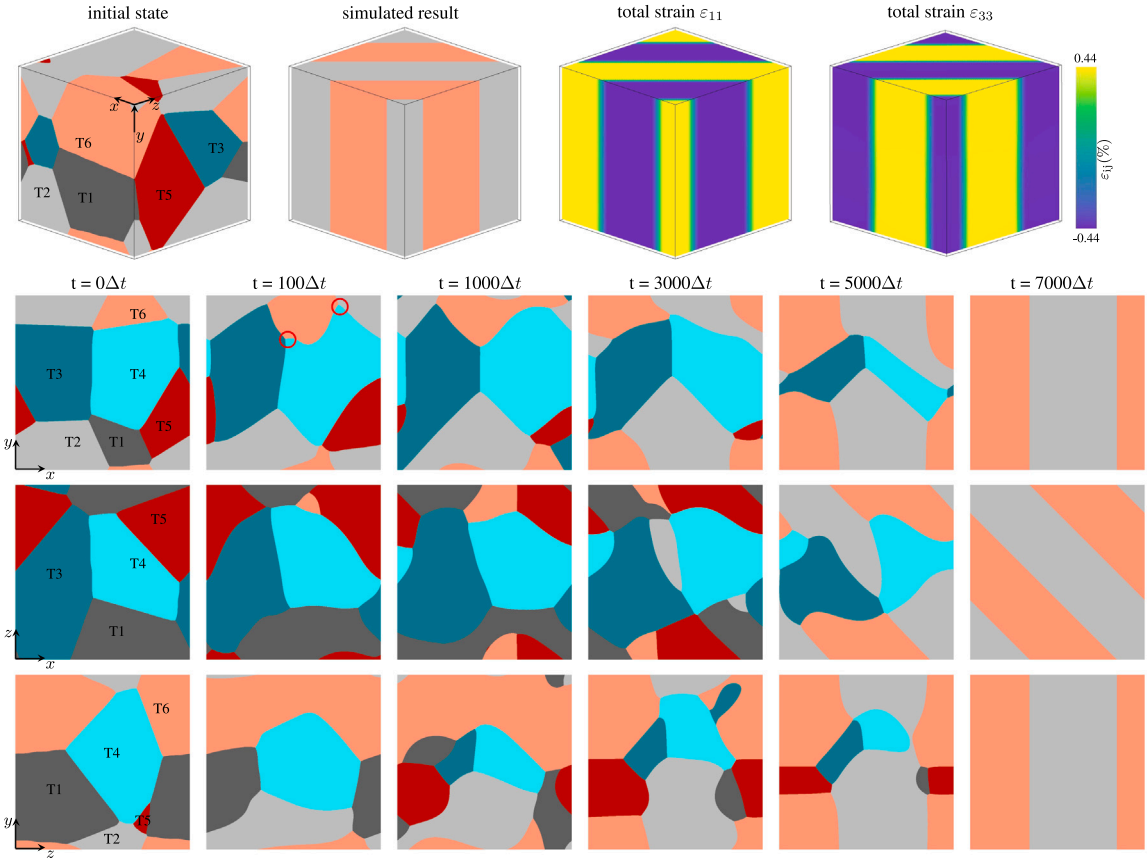

Fig. 3. The simulation of a single crystal in 3D. The first row shows the initial state, the simulated results, and the total strain in 3D. The temporal evolution of the xy-plane at position $z = 50$, of the xz-plane at $y = 50$, and of the yz-plane at $x = 50$ are shown from the second to the fourth row, respectively. The orientation of the polarization for each respective variant can be seen in Fig. 1(d).

steps. It should be large enough to enable the system to eliminate undesired variations at energetically unfavorable nucleation sites, and also small enough to avoid significant effects on the resulting microstructure. Since the applied electric field is along the $[\bar{1}00]$ direction, the formation of T4 variants is energetically more favorable compared to T1 variants. As a result, the T4 variants grow while consuming the T1 phase, which can be observed in Fig. 4(d). Simultaneously, as shown in Figs. 4(d) and (e), the most favorable T2 variants nucleate successfully and grow from the phase boundary, consuming both the T1 and T4 variants. In Fig. 4(f), the system eventually reaches a stable state, characterized by a 90° domain structure composed of T2 and T4 variants.

In contrast, when the same external electric field E^*_{ext} is applied to the x-positive axis, as shown in Fig. 4(g)–(j), it can be observed that even when thermodynamic perturbations are repeatedly caused by the noise $\mathcal{E}$, the T2 and T3 variants do not nucleate. This is due to the fact that the energetically more favorable T1 variant remains stable in the system. In this case, the domain switching was achieved by widening or narrowing the corresponding variants. We also applied the external electric field with the same amplitude along the positive and negative y axes, as shown in Figs. 4(k) and (l). A comparison of Figs. 4 (f) and (k) shows that after switching from the initial structure of the domain (Fig. 2(e)), not only the orientation of the domain changes, but also its size and configuration. This indicates that both 180° and 90° domain switching occurs when the external electric field is aligned with the direction of the absent variants, whereas polarization switching of 90° is observed only when the induced field is parallel to the existing variants (Figs. 4 (j) and (l)). The results calculated with the current model are in agreement with the previous simulations described in Ref. [24], confirming the suitability of our novel phase-field model for the calculation of single crystals under an external electric field.

3.1.3. Polarization and strain hysteresis

The phase-field model for ferroelectric materials should not only allow a qualitative analysis of domain structures, but also a quantitative calculation using an external field. Ferroelectric materials exhibit nonlinear electric and mechanical characteristics with polarization switching. Therefore, in this section, we simulated the polarization and strain hysteresis of the BTO material under the external electric field. Setting Fig. 2(e) as the original state, the induced electric field is parallel (antiparallel) to the positive x-axis, when E_{ext} has a positive (negative) magnitude. Using increments or decrements of 0.24 in strength, the dimensionless E^*_{ext} firstly increased from 0 to 1.2, then decreased from 1.2 to −1.2, followed by another increase from −1.2 to 1.2. To ensure that the calculated structure reaches an equilibrium state, an iteration with a number of 4000 steps was performed at each loading point of the electric field. During the first 1000 steps, the same nucleation mechanism is used at each point. The average polarization $\bar{P}^*_1$ ($\boldsymbol{P}^* = \boldsymbol{P}/|P_0|$) and the average strain $\bar{\varepsilon}_{11}$ in the positive x-axis were considered as the microscopical response of the simulated ferroelectric to the applied electric field. In this simulation, we did not consider the variation of the polarization magnitude under the external field. The calculated PE loop and butterfly are shown in Fig. 5, and the domain configuration of the corresponding points A–G is shown in Fig. 6.

As shown in Figs. 5(a) and (b), starting from the initial state (Fig. 2(e)), the application of an electric field along the positive x-axis results in an increase of both the average polarization and the average strain. The presence of the energy-favorable T1 domains explains the absence of domain nucleation, when comparing Figs. (a) and (e). The change in the domain structure is due to the movement of the domain walls, which leads to the expansion of the T1 variant, at the expense of the T4 variant. Furthermore, the presence of multiple domains

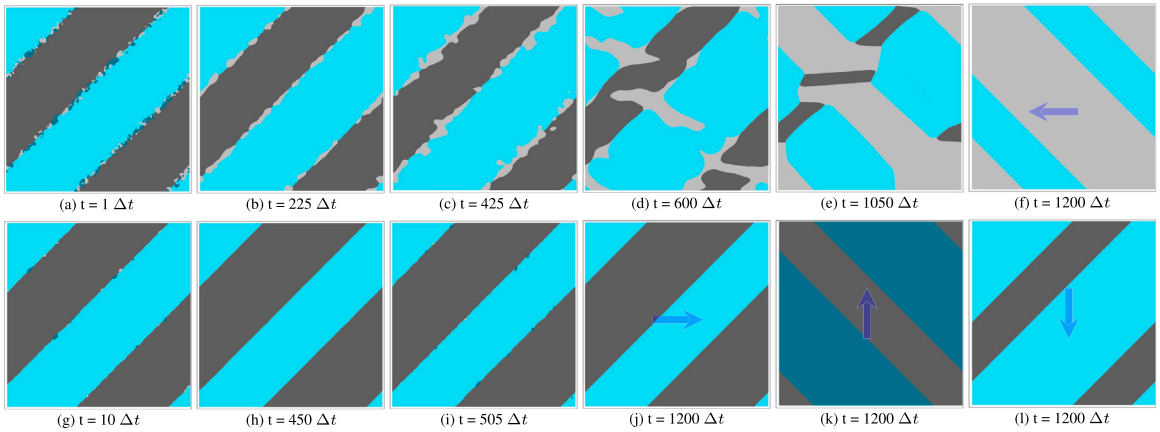

Fig. 4. The simulated results of the domain switching in the application of an external electric field. (a)–(f) shows the temporal evolution of E^*_{ext} applied along the negative x-axis; (g)–(j) shows the temporal evolution of E^*_{ext} applied along the positive x-axis; (k) and (l) show the simulated results of applying E_{ext} along the positive and negative y-axes, respectively. The blue arrows in (f), (j), (k), and (l) represent the direction of the induced electric field.

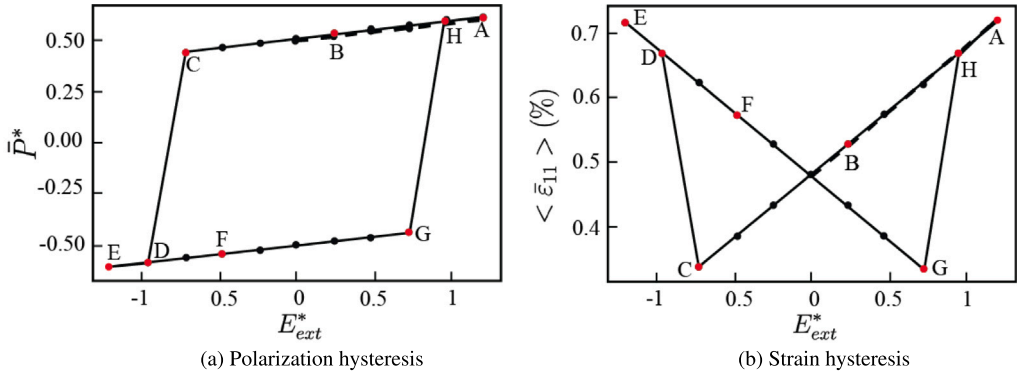

(a) Polarization hysteresis (b) Strain hysteresis

Fig. 5. The simulated polarization and strain hysteresis under the external electric fields.

indicates that point A has not yet reached the saturation state with only one domain configuration. As E^*_{ext} decreases from A to C, both the average polarization and the average strain exhibit a linear decrease (Figs. 5(a)–(c)). Increasing the negative external electric field caused a reversal of the average polarization direction and a significant change in the domain structure, resulting in a jump from point C to D in the comparison between polarization and electric field loop (Fig. 5(a)) and strain and electric field (Fig. 5(b)). Thus, the coercive field can be determined by such a jump. When the negative external electric field strength is increased to point E, the volume fraction of variant T2 in the domain structure increases (as shown in Fig. 6(e)), additionally increasing $\bar{P}^*_1$ and $\bar{\varepsilon}_{11}$, as shown in Fig. 5.

As the applied electric field increases from −1.2 to 1.2, the average polarization increases steadily, while the average strain decreases smoothly from point E to G, as expected. This corresponds to the growth of variant T4 in the domain structure, as shown in Figs. 6(e)–(g). When the electric field reaches the coercive field, the average polarization jumps from negative to positive, while the average strain also jumps, as indicated by points G and H in Fig. 5. This is consistent with the reversal of the polarization direction and the associated change in the domain structure (Figs. 6(g) and (h)). At this stage, we have completed the simulation of the hysteresis loop of the average polarization versus the applied electric field and the average strain versus the applied electric field. It is worth noting that in the current single-crystal simulation, a linear change in the average polarization and average strain results from the assumption of a constant magnitude of polarization ($|P|$ = 26 μC/cm^2), with an increase or decrease in E_{ext} as well as variations in the external electric field.

3.1.4. *Domain switching induced by a mechanical field*

In addition to electric fields, external stress or strain can also induce domain switching, which is another important property of ferroelectric materials. Therefore, in this study, we also calculated the variational transformations induced by an applied strain along the positive x-axis. Fig. 7 shows its temporal evolution of the variants transformation, namely the domain switching, as well as the elastic strain, when a compressive strain $\varepsilon^{ext}_{11} = 0.01$ is applied to Fig. 2(e). It is worth noting that the same approach to nucleation was used in the simulation for external stress- or strain-induced domain switching. However, since the energetically favorable variants were already present in the initial configuration, variants T2 and T3 did not nucleate. This means that the polarization switching induced by a mechanical field is achieved by the movement of the variants already present. Due to this motion, the original tetragonal T1 variant shrinks, while the T4 variant in Fig. 7(a) grows. After 1200 simulation steps, the T4 variant occupies the entire region, resulting in the formation of a single-domain structure. A comparison between the equilibrium structure at 300 steps and the initial structure (0 steps) indicates that only a 90-degree polarization switching occurs under the external strain. Figs. 7(b) and (c) show the temporal evolution of the strain components ε_{11} and ε_{22}, respectively. These plots demonstrate that the 90° polarization switching results in a change in the strain distribution, which in turn reduces the strain energy and minimizes the free energy of the system. Because the 180° polarization switching primarily results from depolarization energy penalties rather than strain energy penalties, there is no nucleation of T2 and T3 variants, which are required for such a domain switching. The simulation results are consistent with those of Wang et al. [24], in

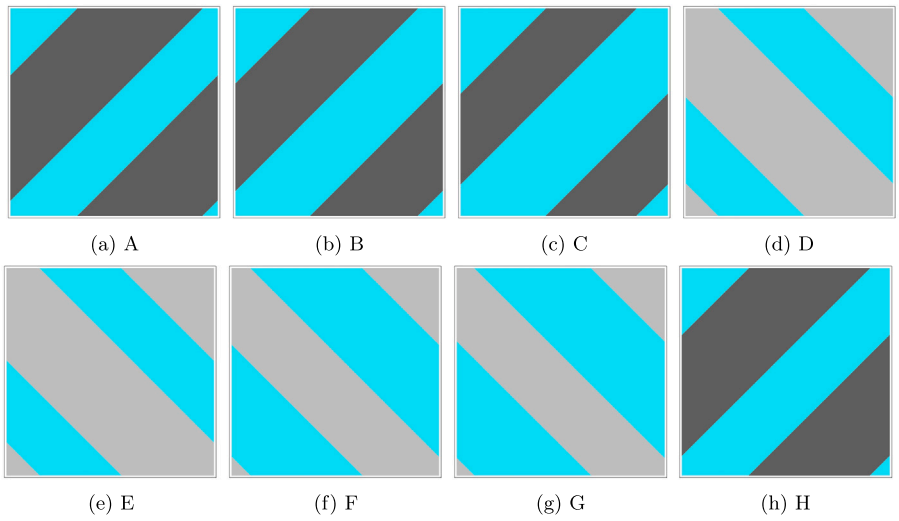

Fig. 6. The domain structures correspond to each point in Fig. 5.

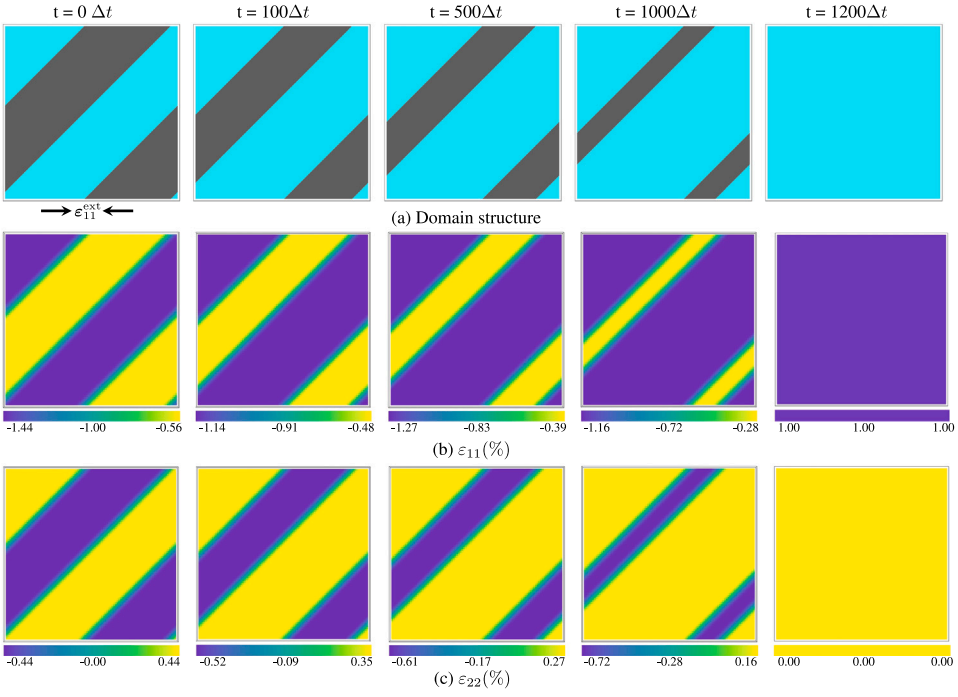

Fig. 7. The temporal evolution of the domain switching (a) and the strains $\varepsilon_{11}(\%)$ (b) as well as $\varepsilon_{22}(\%)$ (c) are shown when the system is subjected to a compressive strain in the x-direction.

which it was found that only 90° polarization switching occurs under external mechanical loading. Meanwhile, the simulation results are consistent with the predictions of continuum theory, which suggest that external mechanical loading can only cause 90° polarization switching in ferroelectric materials.

The results presented above confirm the effectiveness of our proposed model in effectively characterizing the domain formation and switching mechanisms in ferroelectric materials, when exposed to both electric and mechanical fields. In the following section, we explain the practical use of this model for simulating polycrystalline ferroelectric structures.

3.2. Phase-field simulation in polycrystalline systems

3.2.1. Domain formation in bicrystalline structures

To explore the underlying mechanisms of domain formation and domain switching in polycrystalline ferroelectric materials with different orientations, we first performed simulations with four different bicrystalline systems, denoted as B0, B1, B2, and B3. The preliminary configuration of these bicrystalline structures is shown in Fig. 8(a) and shows a quasi-2D structure consisting of 300 × 300 × 1 voxels. Grain orientation within each bicrystalline system is restricted to rotations in the xy-plane. In this context, Grain 2 exhibits no orientation ($\varphi_2 = 0$), while Grain 1 shows unique orientations that correspond to the specific

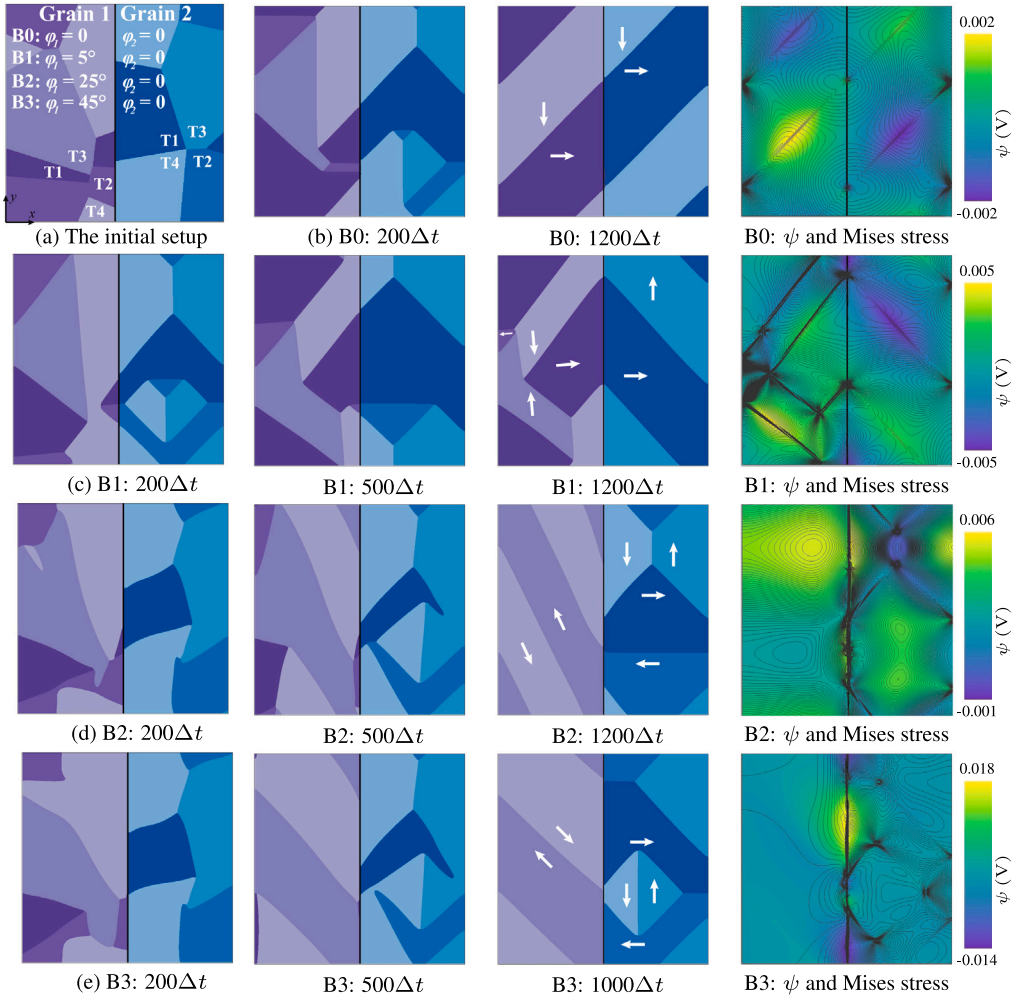

Fig. 8. Simulations of bicrystalline systems, in the absence of an external field. (a) Schematic representation of the bicrystals with specified orientations (B0: $\varphi_1 = 0$, $\varphi_2 = 0$; B1: $\varphi_1 = 5°$, $\varphi_2 = 0$; B2: $\varphi_1 = 25°$, $\varphi_2 = 0$; B3: $\varphi_1 = 45°$, $\varphi_2 = 0$). (b)–(e) show the temporal evolution and distribution of the electric potential (ψ) and the von Mises stress (represented as contour plots with thin black lines) at the stable state for each bicrystalline system. The white arrows in equilibrium represent the direction of the polarization.

bicrystalline system under investigation. Moreover, the grains in each bicrystalline system are composed of four randomly assigned tetragonal variants. The color series in Fig. 8(a) is used to distinguish the grains, with colors ranging from dark to light, indicating the variants T1 to T4. For such a bicrystalline system, we introduced a periodic boundary condition for the phase, electric and mechanical fields along the top and bottom surfaces. To model the behavior of the phase-field $\boldsymbol{\phi}$ at the left and right surface, we applied a homogeneous Neumann boundary condition

$$\frac{\partial \boldsymbol{\phi}}{\partial i}\Big|_{x \in \partial \Omega_i} = 0, \tag{17}$$

in which i stands for the $x-$ or y-direction and $\partial \Omega_i$ is the corresponding field edge. With respect to the depolarization field, a short circuit condition was applied to both the left and right surfaces. Additionally, a clamped boundary condition was employed to compute the mechanical field on the left and right surfaces, which ensured that the displacements in the orthogonal directions were kept to zero. In particular, the mechanical field in the polycrystalline systems, which include both the bicrystalline system and the 10-grain system (which will be discussed in more detail later), is effectively resolved through the application of a mechanical jump condition approach at a diffuse interface, which represents the grain boundary. This approach corresponds to a no-slip mechanical boundary condition, which was also used in Ref. [66] (Eq. (1)) to characterize domain structures in ferroelectric polycrystalline systems.

The simulation of the bicrystals was first performed in the absence of an external field, so as to obtain a stable domain structure. The temporal evolution of the four bicrystals is shown in Figs. 8(b)–(e), where the white arrow in each equilibrium represents the polarization direction of each variant. To illustrate the contribution of the bulk energy, the electric potential as well as a high-density isoline of the von Mises stress (black thin line) in each equilibrium are shown in Figs. 8(b)–(e). For reference, the calculation of a particular grain named B0, with the same initial configuration as in Fig. 8(a), but without any grain orientation, was performed. It should be mentioned that the B0 system differs from the single crystal in that it has a dielectric grain boundary, formed by setting the mobility of the grain boundary to zero. As shown in Fig. 8(b), the simulation results for 200 and 1200 time steps indicate that the absence of grain orientation in each grain across the grain boundary leads to the formation of a continuous 90° domain structure. Specifically, the system initially releases electric energy to avoid the charged domain wall ($t = 200\Delta t$), and subsequently minimizes the elastic energy ($t = 1200\Delta t$), which is in agreement with Section 3.1.1. Despite the formation of a 90° domain wall, the bicrystalline B0 simulation exhibits significant differences in both the electric potential and the von Mises stress (Fig. 8(b)), compared to the single-grain simulation (Fig. 2(f)), which is due to the presence of a grain boundary. Comparing the simulations of the bicrystals B1 to B3, run for 200 iterations, with the initial state (Fig. 2), we see that the system initially releases electrostatic energy to avoid the formation of

tail-to-tail or head-to-head charged domain walls. In bicrystal B1, for example, variant T3 tends to align parallel to variant T4, so as to form a natural 180° domain wall.

The comparison of Figs. 8(b) and 8(c) shows that the grain structure affects the primary simulation process of the variant transformations, resulting in different domain structures in the equilibrium state of B1. For instance, the 5° rotation of Grain 1 stabilized a metastable ferroelectric domain wall constructed by T1 and T2 variants, resulting in a different transformation process for variants in Grain 2 (500 and 1200 iterations in B1). The final equilibrium configuration of B1 reveals that both 180° ferroelectric domain walls and 90° ferroelastic domain walls could be stable in the polycrystalline system, indicating that a 5° rotation in Grain 1 affects the formation of the domain structure. Figs. 8(d) and (e) illustrate the temporal evolution of domain structures in the bicrystals B2 and B3, respectively. In addition to the similar mechanisms described above, it is observed that the grain orientations affect not only the domain structure but also the domain size, leading to the stabilization of different domain structures in Grain 2. This can be seen by comparing the polarization configuration of Grain 2 in the B2 and B3 systems. Moreover, a comparison of the contour plot of the von Mises stress and the electrical potential in the equilibrium state in each grain shows that an increase in the orientation difference between Grain 1 and Grain 2 facilitates the formation of a 180° domain structure in Grain 1. Thus, variant B1 exhibits a dense stress distribution around the domain wall and the numerous junctions of the domains, while the stress in variants B2 and B3 is mainly concentrated on the junctions, due to the natural 180° domains. Such a domain wall plays a crucial role in releasing the electrostatic energy of the system.

3.2.2. Domain switching under an external field in bicrystalline structures

Fig. 9 shows the temporal evolution of the B1 system with an external electric field $E^*_{\text{ext}} = 1$, applied to the equilibrium state of Fig. 8(c), along the negative x-direction, which demonstrates the switching mechanism in such a bicrystalline system with the previously mentioned boundary condition in the current model. Fig. 14 of Appendix C provides additional simulations of the B2 and B3 systems. To simulate the nucleation of the missing variants, a perturbation with a frequency of 50 iterations was introduced during the first 1000 steps. In Fig. 9(a), it is observed that the energetically favorable T2 variant in Grain 1 nucleates between the T1 and T4 variants after 120 iterations, as indicated by the red circle. Subsequently, the nucleated T2 phase grows and propagates to the grain boundary, resulting in the nucleation of another T2 variant in Grain 2, as shown by another red circle in Fig. 9(b). The T2 variant in each grain grew over time by consuming mainly the T1 variant, as shown in Fig. 9(c). However, during the course of the simulation over 800 time steps, this growth resulted in a high energy concentration of both electric and elastic energy in the junction of the different variants at the grain boundary, due to the orientation difference (red circle in Fig. 9(d)). To overcome this energy concentration, a T3 variant nucleated and grew in the grain boundary region, as marked by the right circle in Fig. 9(e). Eventually, as shown in Fig. 9(f), the domain structure switched to two 90° domain walls consisting of T2 and T3 variants in both grains. The polarization direction for each variant is indicated by the white arrows in the image.

In addition to exploring polarization re-orientation under an external electric field, the present study also investigates its response to an external mechanical field. Fig. 10 shows the temporal evolution of the B2 system (the equilibrium state of Fig. 8(d)) subjected to an external strain $\epsilon^{\text{ext}}_{22} = -0.005$ in the y-direction, and Appendix C (Fig. 15) provides detailed simulation results for other bicrystalline systems. With the same simulated parameters as in the above subsection, a simulation of 150 iterations reveals the nucleation of T1 and T2 variants from the grain boundary, as shown in the red circle in Fig. 10(a). As the driving force under such an external strain is the same, T1 and T2 grow equally by consuming the T4 variant (Fig. 10(b)). In general, domain switching is driven by the growth of energetically favorable variants, at the expense of unfavorable variants in the domain wall region, as observed in Fig. 10. This mechanism is similar to the single-grain case (Fig. 7). Furthermore, the domain structure analysis indicates no domain switching in Grain 1, which has a 180° domain wall. This observation suggests that mechanical loading is unable to induce domain switching in the natural domain structures. This finding is also consistent with the simulation results of the B3 system in Fig. 15, which can be found in Appendix C.

3.2.3. Phase-field simulation in the 10-grain polycrystalline material

In this section, we present an illustrative example that demonstrates the domain formation and the calculation of polarization and strain hysteresis in a multigrain system with more than two grains, using the current model. As shown in Fig. 11(a), we consider a 10-grain system consisting of 400 × 400 × 1 voxels rotating randomly on the xy plane. Each grain is uniquely identified by a distinct set of colors. To distinguish between the variants within each grain, we use the same approach as for the bicrystal in Fig. 8(a), where the colors range from dark to light and represent the variants T1 to T4. For the solution of all fields in this simulation, we set a periodic boundary condition.

The process of forming the domain structures in the absence of an external field is primarily illustrated in Figs. 11(b)–(f). In contrast to the initialization of the single-crystal (Fig . 2(a)) and bicrystal systems (Fig. 8(a)), not all variants of this simulation could be assigned to the tetragonal phase, because of the size limitation. To obtain a self-consistent domain structure in equilibrium, we induced the noise $\mathcal{E}$ in Eq. (9) to promote the nucleation of the unassigned variants. In addition, the calculation allows up to 10000 nucleation iterations with a frequency of 200 time steps, which ensures a stable calculation. Figs. 11(b)–(f) mainly show the process of domain formation in such a polycrystalline structure, in which the white arrows represent the polarization direction of each variant. Analogously, the formation of ferroelectric domain walls can facilitate the release of depolarization fields. This mechanism is illustrated by the typical Grains 4 and 5 in Fig. 11(b). In addition, the red circles in Figs. 11(b) and (c) illustrate the nucleation and growth of polarization variants near the grain boundary. This phenomenon occurs when neighboring grains attempt to align their polarization directions, resulting in the release of the built-in depolarization field generated at the grain boundary. The domain structures in such a polycrystalline structure are then formed by the continuous nucleation, growth, and disappearance of polarization variants in each grain driven by the minimization of elastic and electric energy, as shown in Figs. 11(d) and (e). After reaching the equilibrium state, a complex domain structure is formed in the system, characterized by the coexistence of ferroelastic and ferroelectric domain walls, as illustrated in Fig. 11(f). The corresponding electric potential ψ and the von Mises stress of this state are shown in the right image of Fig. 11(f) and represent the contributions of the depolarization and the mechanical field, respectively. In addition to the region of ferroelastic domain walls within each grain, a stress concentration is also observed at the grain boundary, especially in areas with multiple junctions. This observation proves that elastic energy has an influence on the formation of domains in these regions.

Figs. 12(a) and (b) show the calculated polarization and strain hysteresis loop for such a 10-grain system based on the polarization configuration in the equilibrium state (Fig. 11(f)), following the procedure described in Section 3.1.3. To ensure stability at each E_{ext} point in the polycrystalline system, we performed a simulation with 50000 iterations, in contrast to the single-grain simulation. During the first 10000 time steps, we introduced a noise disturbance with a frequency of 200 time steps. The polarization shown (Fig. 12(a)) and the strain (Fig. 12(b)) are each the average value in the x-direction. Similarly, the average polarization generally increases or decreases as the external electric field strength ($|E^*_{\text{ext}}|$) increases or decreases. Interestingly enough, when comparing the simulated polarization and strain hysteresis loops of the single-crystal structure (shown in Fig. 5)

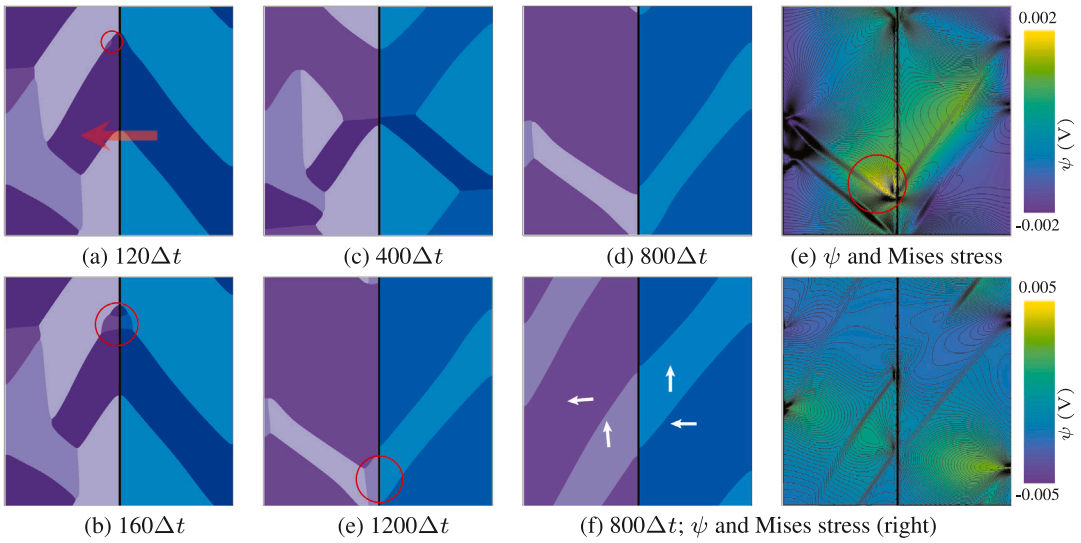

Fig. 9. Temporal evolution of the domain switching in the B1 system upon application of an external electric field of $E^*_{\text{ext}} = 1$ to its equilibrium state shown in Fig. 8(c). The transparent red arrow in (a) shows the direction of the applied field, while the white arrows in the equilibrium state (f) denote the direction of polarization. The right images in (d) and (f) show the corresponding electric potential (ψ) and the von Mises stress (represented as contour plots with thin black lines).

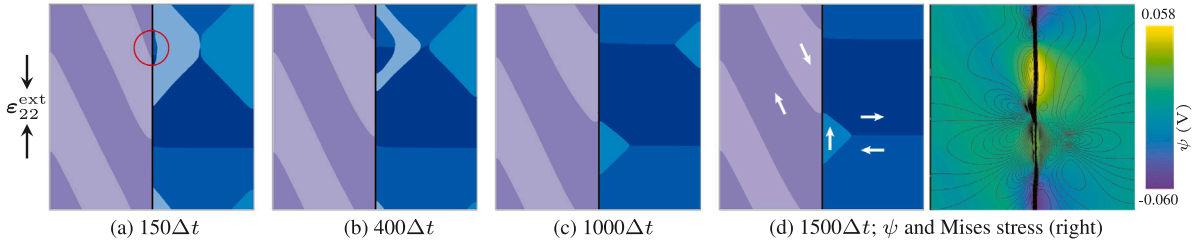

Fig. 10. Temporal evolution of domain switching in the B2 system under a compressive strain $\varepsilon_{22}^{\text{ext}} = 0.005$ was applied to the y-edges. The white arrow in (d) represents the orientation of the polarization, and the right image in (d) shows the electric potential (ψ) and the von Mises stress (shown as contour plots with thin black lines).

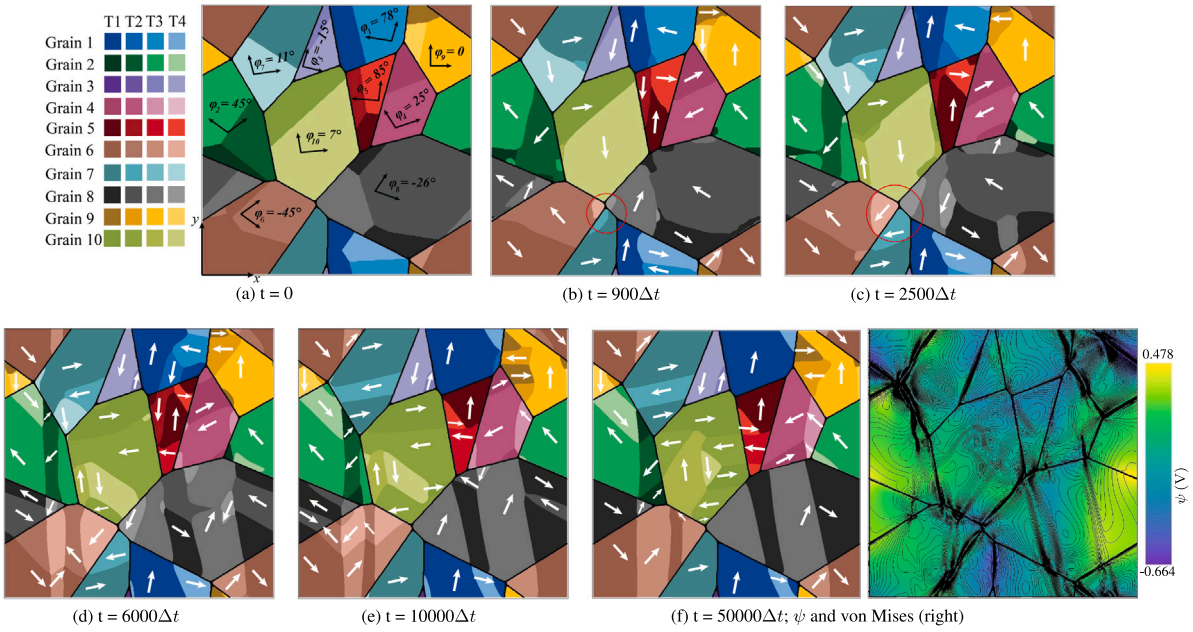

Fig. 11. (a) Initial setting of a polycrystalline structure, (b)–(f) computationally achieved its temporal evolution without applied electric field and mechanical loading. The right image of (f) additionally shows the electric potential ψ and the von Mises stress (black thin line) at the stable state.

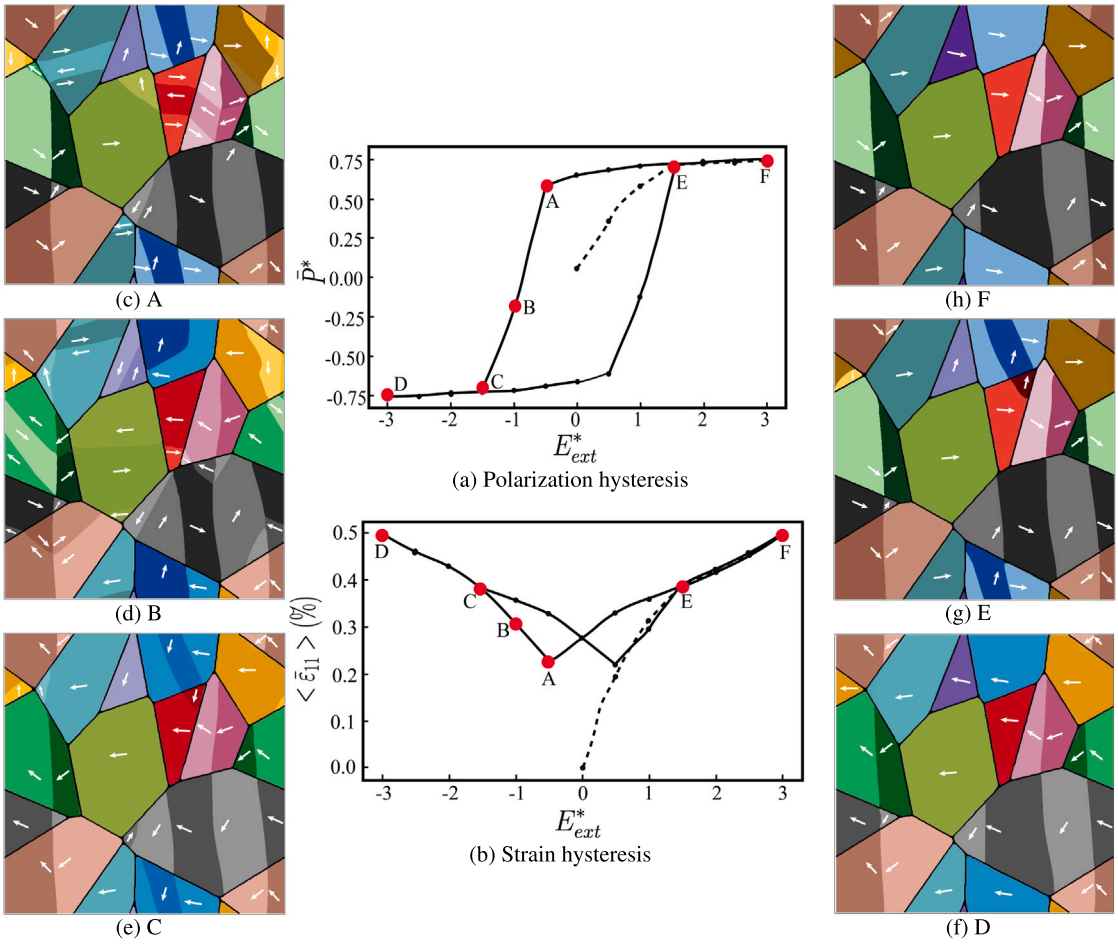

Fig. 12. (a) and (b) show respectively the simulated polarization and strain hysteresis under the induced electric field in the polycrystalline system. The corresponding domain structures for the points A to F in (a) and (b) are shown in the grain structure image in (c)–(h).

and the 10-grain structure (shown in Figs. 12(a)–(b)), a notable finding is that the change in polarization, in response to changes in E^*_{ext}, exhibits nonlinear behavior. This indicates the influence of the grain orientation of the polycrystalline structure on polarization switching. The domain structures in the equilibrium state of the marked points A to F are shown in Figs. 12(c) to (h), where the white arrows represent the polarization direction. When an electric field is applied in the reverse direction, the domain structure of point A, as shown in Fig. 12(c), shows a tendency for the polarization in certain grains to align with the field, especially near the grain boundaries. As the electric field changes from A to C, there is a significant increase in the emergence and growth of domains aligned with the external electric field, as shown in Figs. 12(d) and (e). Notably, such a ferroelectric domain switching results in a considerable jump in polarization and strain, as illustrated in Figs. 12(a) and (b). Similarly, a contrasting jump can be observed when E^*_{ext} is introduced in the positive x-direction (point E), whereby the polarization direction in each grain is once again switched to align with the positive x-direction. The domain structure of the endpoint of the induced polarization loop (point F) is shown in Fig. 12(h), from which it can be seen that the polarization orientation in each grain aligns with the external electric field and the respective crystal orientation. However, analogous to point C, the presence of multi-domain structures within certain grains indicates that saturation polarization has not yet been reached in the current simulation.

As a brief summary, this section provides examples to illustrate the mechanisms of domain formation and switching under an external field in polycrystalline ferroelectric materials, using the multiphase-field approach. In general, the nucleation of variants at the beginning of the simulations is necessary to achieve a self-consistent domain structure for complex polycrystalline systems, in the absence of an external field. However, for simple multigrain systems where all variants can be assigned within each grain, nucleation is usually omitted to improve the efficiency of the calculation. Similar to simulations in single crystals, the inclusion of nucleation mechanisms enables domain switching under external fields in polycrystalline systems. Therefore, the current model also allows the calculation of polarization and strain hysteresis in polycrystalline systems.

4. Conclusion

We have developed a 3D phase-field model that includes a multiphase and multicomponent phase-field functional to calculate domain structures and material properties in both single- and polycrystalline ferroelectric materials, under stimulated and non-stimulated conditions. Our model defines the possible polarization variation in each ferroelectric phase as a phase ϕ_α. The movement of the diffusion interface between the phases drives the formation of the domain structures. In this paper, we have used $BaTiO_3$ as a model material to demonstrate the calculation of a domain structure and domain switching, using the current model in both single and polycrystalline systems. In general, the domain formation in a single crystal or a simple multigrain system can be calculated without considering noise perturbations, if no external field is present, and each polarization assignment can be easily determined using the Voronoi approach. However, to accurately model polarization switching under external fields, it is necessary to introduce a noise term into the governing function (Eq. (9)) to account

for the nucleation of missing polarization variants near domain walls or grain boundaries. Furthermore, in the case of a complex polycrystalline structure where the dimension limits the assignment of all polarization variants of the ferroelectric phase in each grain, the nucleation mechanism is also implemented at the beginning of the simulation to achieve a self-consistent domain configuration during the domain formation process. Based on this, the material properties such as the polarization and strain hysteresis loop under the external electric fields are calculated in both a single crystal and a 10-grain system. In the present study, it should be emphasized that the noise term is integrated to represent the nucleation process since the potential was assumed to be of the multi-obstacle type. Conversely, when using a multiwell methodology, the inclusion of the noise term may not be considered necessary. In general, our results are consistent with the existing literature, which verifies the feasibility and reliability of our model. This work serves as an essential reference for the further development of the multiphase concept in ferroelectric materials.

CRediT authorship contribution statement

Ling Fan: Methodology, Conceptualization, Formal analysis, Validation, Visualization, Writing – original draft, Writing – review & editing. **Martin Reder:** Software, Writing – review & editing. **Daniel Schneider:** Methodology, Conceptualization, Writing – review & editing. **Manuel Hinterstein:** Methodology, Conceptualization, Writing – review & editing. **Britta Nestler:** Supervisor, Writing – review & editing, Funding acquisition.

Declaration of competing interest

The authors declare that they have no known competing financial interests or personal relationships that could have appeared to influence the work reported in this paper.

Data availability

Data will be made available on request.

Acknowledgments

The multiphase-field model with combined electric potential and integrated noise formulation was composed through the grant of the Zeiss project "Kera Solar", which is gratefully acknowledged. A combination of the microstructure model with mechanical energy contributions was supported as part of the program "Materials Systems Engineering (MSE)", 43.31.01 of the Helmholtz Association. Additionally, this work is funded by the *Bundesministerium für Bildung und Forschung* (BMBF), Germany within the KMU-innovative project BioSorb. Ling Fan expresses gratitude for the financial support received from the China Scholarship Council. Manuel Hinterstein thanks the "Deutsche Forschungsgemeinschaft" (DFG), Germany for financial support under grant no. HI 1867/1-2 and the Fraunhofer Internal Programs under grant no. Attract 40-04857. The authors would like to thank the state of Baden-Württemberg for their support, as part of the bwHPC program. Lastly, the authors express their gratitude towards Leon Geisen for his contribution to improving the English language of this manuscript.

Appendix A. Multiphase elasticity model

The primary concept of the jump condition method is to transform the stresses and strains to the basis $\boldsymbol{B}$, which is defined by the local vector $\boldsymbol{n}$ ($\boldsymbol{n} = \frac{\nabla L(\boldsymbol{\phi})}{|\nabla L(\boldsymbol{\phi})|}$, with $L(\boldsymbol{\phi}) = \sum_{\alpha<\beta} \phi^\alpha \phi^\beta$), followed by the energy calculation with only homogeneous variables from the jump condition method [6,52]. Subjected to the constraints $\boldsymbol{n}\cdot\boldsymbol{t} = \boldsymbol{n}\cdot\boldsymbol{s} = \boldsymbol{t}\cdot\boldsymbol{s} = 0$, the basis $\boldsymbol{B}$ takes the configuration $\boldsymbol{B} = (\boldsymbol{n}, \boldsymbol{t}, \boldsymbol{s})$. Using the Voigt notation, the stress and strain within $\boldsymbol{B}$ can be expressed as:

$$\begin{aligned}\boldsymbol{\sigma}_{\boldsymbol{B}}^{\alpha} &:= \left(\sigma_{nn}, \sigma_{nt}, \sigma_{ns}, \sigma_{tt}, \sigma_{ss}\, \sigma_{ts}\right)^{\mathrm{T}} = (\boldsymbol{\sigma}_n, \boldsymbol{\sigma}_t^{\alpha})^{\mathrm{T}},\\ \boldsymbol{\varepsilon}_{\boldsymbol{B}}^{\alpha} &:= \left(\varepsilon_{nn}, 2\varepsilon_{nt}, 2\varepsilon_{ns}, \varepsilon_{tt}, 2\varepsilon_{ss}\, \varepsilon_{ts}\right)^{\mathrm{T}} = (\boldsymbol{\varepsilon}_n^{\alpha}, \boldsymbol{\varepsilon}_t)^{\mathrm{T}}.\end{aligned} \tag{A.1}$$

Depending on the force balance $[\![\boldsymbol{\sigma}_n]\!] = \boldsymbol{0}$ and the Hadamard condition $[\![\boldsymbol{\varepsilon}_t]\!] = \boldsymbol{0}$ for an infinitesimal deformation at a singular plane, the stress and strain can be reordered as continuous, $\boldsymbol{\sigma}_n := (\sigma_{nn}, \sigma_{nt}, \sigma_{ns})^{\mathrm{T}}$, $\boldsymbol{\varepsilon}_t := (\varepsilon_{tt}, \varepsilon_{ss}, \varepsilon_{ts})^{\mathrm{T}}$, and discontinuous, $\boldsymbol{\sigma}_t^{\alpha} := (\sigma_{tt}, \sigma_{ss}\, \sigma_{ts})^{\mathrm{T}}$, $\boldsymbol{\varepsilon}_n^{\alpha} := (\varepsilon_{nn}, 2\varepsilon_{nt}, 2\varepsilon_{ns})^{\mathrm{T}}$, contributions. Following Refs. [50,52], the stiffness tensor $\boldsymbol{C}_{\boldsymbol{B}}^{\alpha}$ corresponding to phase α in basis $\boldsymbol{B}$ is represented as follows, using the Voigt notation:

$$\boldsymbol{C}_{\boldsymbol{B}}^{\alpha} := \begin{bmatrix} \boldsymbol{C}_{nn}^{\alpha} & \boldsymbol{C}_{nt}^{\alpha} \\ \boldsymbol{C}_{tn}^{\alpha} & \boldsymbol{C}_{tt}^{\alpha} \end{bmatrix} = \left[\begin{array}{ccc|ccc} C_{nnnn}^{\alpha} & C_{nnnt}^{\alpha} & C_{nnns}^{\alpha} & C_{nntt}^{\alpha} & C_{nnss}^{\alpha} & C_{nnts}^{\alpha} \\ C_{ntnn}^{\alpha} & C_{ntnt}^{\alpha} & C_{ntns}^{\alpha} & C_{nttt}^{\alpha} & C_{ntss}^{\alpha} & C_{ntts}^{\alpha} \\ C_{nsnn}^{\alpha} & C_{nsnt}^{\alpha} & C_{nsns}^{\alpha} & C_{nstt}^{\alpha} & C_{nsss}^{\alpha} & C_{nsts}^{\alpha} \\ \hline C_{ttnn}^{\alpha} & C_{ttnt}^{\alpha} & C_{ttns}^{\alpha} & C_{tttt}^{\alpha} & C_{ttss}^{\alpha} & C_{ttts}^{\alpha} \\ C_{ssnn}^{\alpha} & C_{ssnt}^{\alpha} & C_{ssns}^{\alpha} & C_{sstt}^{\alpha} & C_{ssss}^{\alpha} & C_{ssts}^{\alpha} \\ C_{tsnn}^{\alpha} & C_{tsnt}^{\alpha} & C_{tsns}^{\alpha} & C_{tstt}^{\alpha} & C_{tsss}^{\alpha} & C_{tsts}^{\alpha} \end{array}\right]. \tag{A.2}$$

In this context, $\boldsymbol{C}_{nn}^{\alpha}$ and $\boldsymbol{C}_{tt}^{\alpha}$ are symmetric 3×3 matrices, while $\boldsymbol{C}_{nt}^{\alpha}$ and $\boldsymbol{C}_{tn}^{\alpha}$ are 3×3 matrices that satisfy the requisite condition $\boldsymbol{C}_{nt}^{\alpha} = [\boldsymbol{C}_{tn}^{\alpha}]^{\mathrm{T}}$. Similarly, a proportionality matrix $\tilde{\boldsymbol{\mathcal{T}}}^{\alpha}$ is introduced as follows, which is later involved in the formation of the elastic potential:

$$\tilde{\boldsymbol{\mathcal{T}}}^{\alpha} = \begin{pmatrix} \tilde{\boldsymbol{\mathcal{T}}}_{nn}^{\alpha} & \tilde{\boldsymbol{\mathcal{T}}}_{nt}^{\alpha} \\ \tilde{\boldsymbol{\mathcal{T}}}_{tn}^{\alpha} & \tilde{\boldsymbol{\mathcal{T}}}_{tt}^{\alpha} \end{pmatrix}, \tag{A.3}$$

within which each element of $\tilde{\boldsymbol{\mathcal{T}}}^{\alpha}$ corresponds to an interpolated block and reads:

$$\begin{aligned}\boldsymbol{\mathcal{T}}_{nn}^{\alpha} &:= -(\boldsymbol{C}_{nn}^{\alpha})^{-1}\\ \boldsymbol{\mathcal{T}}_{nt}^{\alpha} &:= -(\boldsymbol{C}_{nn}^{\alpha})^{-1}\boldsymbol{C}_{nt}^{\alpha}\\ \boldsymbol{\mathcal{T}}_{tt}^{\alpha} &:= -\left(\boldsymbol{C}_{tt}^{\alpha} - \boldsymbol{C}_{tn}^{\alpha}(\boldsymbol{C}_{nn}^{\alpha})^{-1}\boldsymbol{C}_{nt}^{\alpha}\right).\end{aligned} \tag{A.4}$$

The elastic free energy density of phase α, based on the strain components in basis $\boldsymbol{B}$, is given by:

$$\begin{aligned}f^{\alpha}(\boldsymbol{\varepsilon}_{\boldsymbol{B}}^{\alpha}) = \frac{1}{2}\Big[\, &(\boldsymbol{\varepsilon}_n^{\alpha} - \tilde{\boldsymbol{\varepsilon}}_n^{\alpha})\cdot\boldsymbol{C}_{nn}^{\alpha}(\boldsymbol{\varepsilon}_n^{\alpha} - \tilde{\boldsymbol{\varepsilon}}_n^{\alpha}) + (\boldsymbol{\varepsilon}_n^{\alpha} - \tilde{\boldsymbol{\varepsilon}}_n^{\alpha})\cdot\boldsymbol{C}_{nt}^{\alpha}(\boldsymbol{\varepsilon}_t^{\alpha} - \tilde{\boldsymbol{\varepsilon}}_t^{\alpha})\\ &+ (\boldsymbol{\varepsilon}_t^{\alpha} - \tilde{\boldsymbol{\varepsilon}}_t^{\alpha})\cdot\boldsymbol{C}_{tn}^{\alpha}(\boldsymbol{\varepsilon}_n^{\alpha} - \tilde{\boldsymbol{\varepsilon}}_n^{\alpha}) + (\boldsymbol{\varepsilon}_t^{\alpha} - \tilde{\boldsymbol{\varepsilon}}_t^{\alpha})\cdot\boldsymbol{C}_{tt}^{\alpha}(\boldsymbol{\varepsilon}_t^{\alpha} - \tilde{\boldsymbol{\varepsilon}}_t^{\alpha})\,\Big].\end{aligned} \tag{A.5}$$

Referring to [50], the elastic potential W in Eq. (11) reads as:

$$\begin{aligned}W(\boldsymbol{\varepsilon}_t, \boldsymbol{\sigma}_n, \boldsymbol{\phi}) = \sum\nolimits_{\alpha}\Bigg[&\begin{pmatrix}\boldsymbol{\sigma}_n\\ \boldsymbol{\varepsilon}_t\end{pmatrix}\cdot\tilde{\boldsymbol{\mathcal{T}}}^{\alpha}\begin{pmatrix}\boldsymbol{\sigma}_n\\ \boldsymbol{\varepsilon}_t\end{pmatrix} - \begin{pmatrix}\boldsymbol{\sigma}_n\\ \boldsymbol{\varepsilon}_t\end{pmatrix}\cdot\begin{pmatrix}\boldsymbol{I} & \boldsymbol{\mathcal{T}}_{nt}^{\alpha}\\ \boldsymbol{0} & \boldsymbol{\mathcal{T}}_{tt}^{\alpha}\end{pmatrix}\begin{pmatrix}\tilde{\boldsymbol{\varepsilon}}_n^{\alpha}\\ \tilde{\boldsymbol{\varepsilon}}_t^{\alpha}\end{pmatrix}\\ &+ \frac{1}{2}\left(\tilde{\boldsymbol{\varepsilon}}_t^{\alpha}\cdot\boldsymbol{\mathcal{T}}_{tt}^{\alpha}\tilde{\boldsymbol{\varepsilon}}_t^{\alpha}\right)\Bigg] h^{\alpha}(\boldsymbol{\phi}).\end{aligned} \tag{A.6}$$

$\boldsymbol{I}$ and $\boldsymbol{0}$ are second-order identity and zero tensors, respectively. To gain a full understanding of the jump condition method used in the multiphase-field model, the reader is strongly encouraged to consult Refs. [6,16,52].

Appendix B. The dimensionless approach

When considering the simulation parameters for the tetragonal interface in BTO material, we refer to the literature [22]. Specifically, we require the values of α_1 and G_{11}, which are expressed in units of $\mathrm{N\,m^2/C^2}$ and $\mathrm{N\,m^4/C^2}$, respectively. We choose a spatial step size of $\Delta x = 0.5\,\mathrm{nm}$, which approximates $\sqrt{G_{110}/|\alpha_1|}$, assuming that $G_{110} = G_{11} = 3.46\times 10^{-10}\ \mathrm{N\,m^4/C^2}$. As no reliable data is available for the kinetics of the tetragonal domain wall, we set the discrete time step width Δt^*=1 and determine the mobility $M_{\alpha\beta}$ between the tetragonal variants to ensure numerical stability. In general, the main dimensionless formulas are:

$$Q_{ijkl}^{*} = Q_{ijkl}P_0^2, \qquad C_{ijkl}^{*} = \frac{C_{ijkl}}{|\alpha_1 P_0^2|}, \qquad \kappa_0^{*} = \kappa\cdot|\alpha_1| \tag{B.1}$$

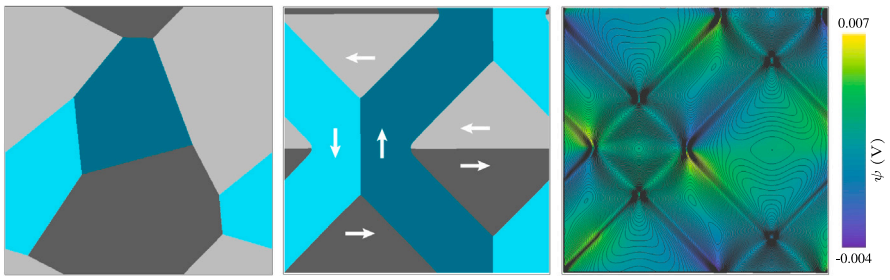

(a) Initial setup (b) Stable state (c) ψ and Von Mises stress

Fig. 13. Domain structure in a single-crystal structure. (a) The initial state of a 2D single crystal with 500 × 500 × 1 cells and its corresponding polarization configuration in the equilibrium state (b). The white arrows in (b) represent the direction of the polarization. (c) The electric potential ψ and the distribution of the von Mises stress (the black thin line) in the stable state.

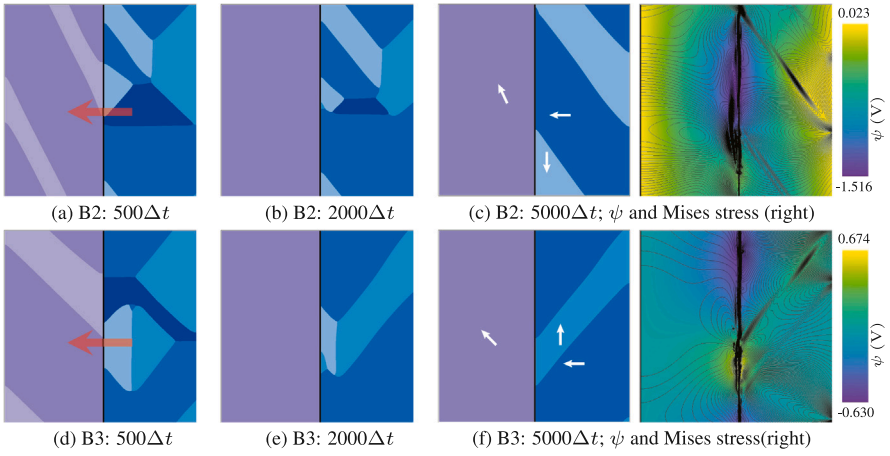

(a) B2: $500\Delta t$ (b) B2: $2000\Delta t$ (c) B2: $5000\Delta t$; ψ and Mises stress (right)

(d) B3: $500\Delta t$ (e) B3: $2000\Delta t$ (f) B3: $5000\Delta t$; ψ and Mises stress(right)

Fig. 14. Temporal evolution of the domain structures in the B2 and B3 system, upon application of an external electric field of $E^*_{\text{ext}} = 1$ to their equilibrium state, shown in Figs. 8(d) and (e). The transparent red arrows in (a) and (d) indicate the direction of the applied field, while the white arrows in the equilibrium state (c) and (f) indicate the direction of polarization. In (c) and (f), the images on the right show the corresponding electric potential (ψ) and the von Mises stress (shown as contour plots with thin black lines).

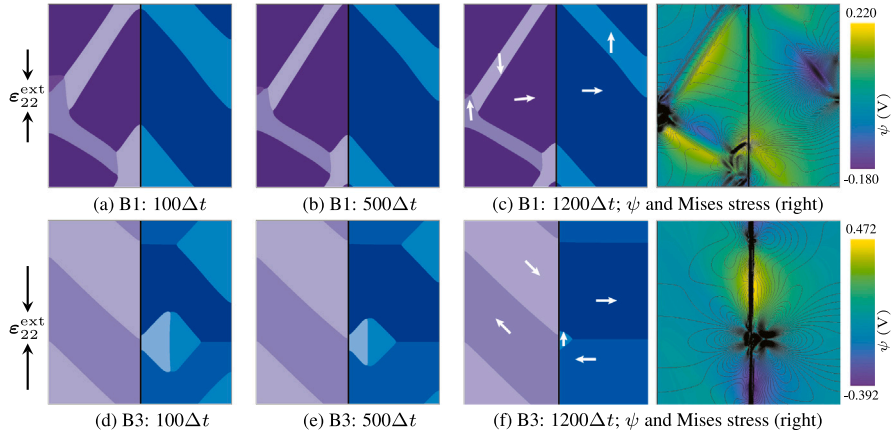

(a) B1: $100\Delta t$ (b) B1: $500\Delta t$ (c) B1: $1200\Delta t$; ψ and Mises stress (right)

(d) B3: $100\Delta t$ (e) B3: $500\Delta t$ (f) B3: $1200\Delta t$; ψ and Mises stress (right)

Fig. 15. The temporal evolution of domain structures in B1 and B3 systems under a compressive strain $\epsilon^{\text{ext}}_{22} = 0.005$ was applied to the y-edges. The white arrow in (c) and (d) represents the orientation of the polarization. In (c) and (f), the images on the right illustrate the electric potential (ψ) and the von Mises stress (shown as contour plots with thin black lines).

Appendix C. Simulated domain structures

See Figs. 13–15.

References

[1] A.A Wheeler, W.J Boettinger, G.B McFadden, Phase-field model for isothermal phase transitions in binary alloys, Phys. Rev. A 45 (10) (1992) 7424.

[2] J.A Warren, W.J Boettinger, Prediction of dendritic growth and microsegregation patterns in a binary alloy using the phase-field method, Acta Metall. Mater. 43 (2) (1995) 689–703.

[3] B. Echebarria, R. Folch, A. Karma, M. Plapp, Quantitative phase-field model of alloy solidification, Phys. Rev. E 70 (6) (2004) 061604.

[4] B. Nestler, A. Choudhury, Phase-field modeling of multi-component systems, Curr. Opin. Solid State Mater. Sci. 15 (3) (2011) 93–105.

[5] E. Schoof, D. Schneider, N. Streichhan, T. Mittnacht, M. Selzer, B. Nestler, Multiphase-field modeling of martensitic phase transformation in a dual-phase microstructure, Int. J. Solids Struct. (2017).

[6] E. Schoof, D. Schneider, N. Streichhan, T. Mittnacht, M. Selzer, B. Nestler, Multiphase-field modeling of martensitic phase transformation in a dual-phase microstructure, Int. J. Solids Struct. 134 (2018) 181–194.

[7] S. Daubner, M. Weichel, D. Schneider, B. Nestler, Modeling intercalation in cathode materials with phase-field methods: Assumptions and implications using the example of LiFePO4, Electrochim. Acta 421 (2022) 140516.

[8] Y Zeng, T Mittnacht, W Werner, Y Du, D Schneider, B Nestler, Gibbs energy and phase-field modeling of ferromagnetic ferrite (α)→ paramagnetic austenite (γ) transformation in Fe–C alloys under an external magnetic field, Acta Mater. 225 (2022) 117595.

[9] Y. Wang, L.-Q. Chen, A.G. Khachaturyan, Kinetics of strain-induced morphological transformation in cubic alloys with a miscibility gap, Acta Mater. 41 (1) (1993) 279–296.

[10] J.Z. Zhu, T. Wang, A.J. Ardell, S.H. Zhou, Z.K. Liu, L.Q. Chen, Three-dimensional phase-field simulations of coarsening kinetics of γ particles in binary Ni–Al alloys, Acta Mater. 52 (9) (2004) 2837–2845.

[11] V. Vaithyanathan, L.-Q. Chen, Coarsening kinetics of δ-Al_3Li precipitates: phase-field simulation in 2D and 3D, Scr. Mater. 42 (10) (2000) 967–973.

[12] D. Jacqmin, Calculation of two-phase Navier–Stokes flows using phase-field modeling, J. Comput. Phys. 155 (1) (1999) 96–127.

[13] M. Reder, D. Schneider, F. Wang, S. Daubner, B. Nestler, Phase-field formulation of a fictitious domain method for particulate flows interacting with complex and evolving geometries, Internat. J. Numer. Methods Fluids 93 (8) (2021) 2486–2507.

[14] M. Reder, P.W Hoffrogge, D. Schneider, B. Nestler, A phase-field based model for coupling two-phase flow with the motion of immersed rigid bodies, Int. J. Numer. Methods Eng. 93 (8) (2022) 2486–2507.

[15] D. Schneider, M. Selzer, J. Bette, I. Rementeria, A. Vondrous, M.J. Hoffmann, B. Nestler, Phase-field modeling of diffusion coupled crack propagation processes, Adv. Eng. Mater. 16 (2) (2014) 142–146.

[16] D. Schneider, Stefan Schmid, M. Selzer, T. Böhlke, B. Nestler, Small strain elasto-plastic multiphase-field model, Comput. Mech. 55 (1) (2015) 27–35.

[17] D. Schneider, E. Schoof, Y. Huang, M. Selzer, B. Nestler, Phase-field modeling of crack propagation in multiphase systems, Comput. Methods Appl. Mech. Engrg. 312 (2016) 186–195.

[18] L. Schöller, D. Schneider, C. Herrmann, A. Prahs, B. Nestler, Phase-field modeling of crack propagation in heterogeneous materials with multiple crack order parameters, Comput. Methods Appl. Mech. Engrg. 395 (2022) 114965.

[19] M. Späth, C. Herrmann, N. Prajapati, F. Schneider, M. Selzer, B. Nestler, Multiphase-field modelling of crack propagation in geological materials and porous media with Drucker-Prager plasticity, Comput. Geosci. 25 (1) (2021) 325–343.

[20] W. Cao, L.E. Cross, Theory of tetragonal twin structures in ferroelectric perovskites with a first-order phase transition, Phys. Rev. B 44 (1) (1991) 5.

[21] S. Nambu, D.A Sagala, Domain formation and elastic long-range interaction in ferroelectric perovskites, Phys. Rev. B 50 (9) (1994) 5838.

[22] H.L. Hu, L.Q. Chen, Three-dimensional computer simulation of ferroelectric domain formation, J. Am. Ceram. Soc. 81 (3) (1998) 492–500.

[23] Y.L. Li, S.Y. Hu, Z.K. Liu, L.Q. Chen, Effect of electrical boundary conditions on ferroelectric domain structures in thin films, Appl. Phys. Lett. 81 (3) (2002) 427–429.

[24] J. Wang, S.Q. Shi, L.Q. Chen, Y.L. Li, T.Y. Zhang, Phase-field simulations of ferroelectric/ferroelastic polarization switching, Acta Mater. 52 (2004).

[25] L.Q. Chen, Phase-field method of phase transitions/domain structures in ferroelectric thin films: a review, J. Am. Ceram. Soc. 91 (6) (2008) 1835–1844.

[26] J.J. Wang, B. Wang, L.Q. Chen, Understanding, predicting, and designing ferroelectric domain structures and switching guided by the phase-field method, Annu. Rev. Mater. Res. 49 (2019) 127–152.

[27] S. Choudhury, Y.L. Li, C.E. Krill Iii, L.Q. Chen, Phase-field simulation of polarization switching and domain evolution in ferroelectric polycrystals, Acta Mater. 53 (20) (2005) 5313–5321.

[28] S. Choudhury, Y.L. Li, C. Krill Iii, L.Q. Chen, Effect of grain orientation and grain size on ferroelectric domain switching and evolution: Phase field simulations, Acta Mater. 55 (4) (2007) 1415–1426.

[29] J. Wang, W.L. Shu, T. Shimada, T. Kitamura, T.Y. Zhang, Role of grain orientation distribution in the ferroelectric and ferroelastic domain switching of ferroelectric polycrystals, Acta Mater. 61 (16) (2013) 6037–6049.

[30] Y. Xiao, V.B Shenoy, K. Bhattacharya, Depletion layers and domain walls in semiconducting ferroelectric thin films, Phys. Rev. Lett. 95 (24) (2005) 247603.

[31] T. Sluka, A.K Tagantsev, D. Damjanovic, M. Gureev, N. Setter, Enhanced electromechanical response of ferroelectrics due to charged domain walls, Nature Commun. 3 (1) (2012) 1–7.

[32] Y.-S. Teh, K. Bhattacharya, Photovoltaic effect in multi-domain ferroelectric perovskite oxides, J. Appl. Phys. 125 (6) (2019) 064103.

[33] Y. Ji, W.J. Chen, Y. Zheng, The emergence of tunable negative electrocaloric effect in ferroelectric/paraelectric superlattices, J. Phys. D Appl. Phys. 53 (50) (2020) 505302.

[34] Z. Hong, A.R. Damodaran, F. Xue, S.L. Hsu, J. Britson, A.K. Yadav, C.T. Nelson, J.J. Wang, J.F. Scott, L.W. Martin, R. Ramesh, L.-Q. Chen, Stability of polar vortex lattice in ferroelectric superlattices, Nano Lett. 17 (4) (2017) 2246–2252.

[35] J.J. Wang, T.N. Yang, J.A. Zorn, E Wang, J Irwin, S Lindemann, M.S. Rzchowski, J.M Hu, C.B. Eom, L.Q. Chen, Strain anisotropy and magnetic domain structures in multiferroic heterostructures: High-throughput finite-element and phase-field studies, Acta Mater. 176 (2019) 73–83.

[36] Y. Ji, W.J. Chen, Y. Zheng, Crossover of polar and toroidal orders in ferroelectric nanodots with a morphotropic phase boundary and nonvolatile polar-vortex transformations, Phys. Rev. B 100 (1) (2019) 014101.

[37] J. Wang, M. Kamlah, T.-Y. Zhang, Y. Li, L.-Q. Chen, Size-dependent polarization distribution in ferroelectric nanostructures: Phase field simulations, Appl. Phys. Lett. 92 (16) (2008) 162905.

[38] D. Fan, C. Geng, L.-Q. Chen, Computer simulation of topological evolution in 2-D grain growth using a continuum diffuse-interface field model, Acta Mater. 45 (3) (1997) 1115–1126.

[39] J. Tiaden, B. Nestler, H.-J. Diepers, I. Steinbach, The multiphase-field model with an integrated concept for modelling solute diffusion, Phys. D: Nonlinear Phenom. 115 (1–2) (1998) 73–86.

[40] B. Nestler, H. Garcke, B. Stinner, Multicomponent alloy solidification: Phase-field modeling and simulations, Phys. Rev. E 71 (4) (2005) 041609.

[41] I. Steinbach, Phase-field models in materials science, Modelling Simul. Mater. Sci. Eng. 17 (7) (2009) 073001.

[42] O.A. Torres-Matheus, R.E. García, C.M. Bishop, Phase coexistence near the polymorphic phase boundary, Acta Mater. 164 (2019) 577–585.

[43] O.A. Torres Matheus, Multiphase Field Modelling of Ferroelectric Materials near the Polymorphic Phase Boundary (Ph.D. thesis), University of Canterbury, 2020.

[44] O.A. Torres-Matheus, R.E. García, C.M. Bishop, Microstructural phase coexistence kinetics near the polymorphic phase boundary, Acta Mater. 206 (2021) 116579.

[45] O.A. Torres-Matheus, R.E. García, C.M. Bishop, Physics-based optimization of Landau parameters for ferroelectrics: application to BZT–50BCT, Modelling Simul. Mater. Sci. Eng. 29 (7) (2021) 075001.

[46] L. Fan, W. Werner, S. Subotić, D. Schneider, M. Hinterstein, B. Nestler, Multigrain phase-field simulation in ferroelectrics with phase coexistences: An improved phase-field model, Comput. Mater. Sci. 203 (2022) 111056.

[47] Q. Chen, Y. Zhang, W. Liu, J. Jiang, Q. Yang, L. Jiang, Ferroelectric switching behavior of nanoscale $Hf_{0.5}Zr_{0.5}O_2$ grains, Int. J. Mech. Sci. 212 (2021) 106828.

[48] B. Lai, Y. Wang, Y. Shao, Y. Deng, W. Yang, L. Jiang, Y. Zhang, Study on the phase transition dynamics of HfO_2-based ferroelectric films under ultrafast electric pulse, J. Phys. Condens. 33 (40) (2021) 405402.

[49] L. Guin, D. Kochmann, A phase-field model for ferroelectrics with general kinetics. Part I: Model formulation, 2022, arXiv:2203.16479.

[50] D. Schneider, O. Tschukin, A. Choudhury, M. Selzer, T. Böhlke, B. Nestler, Phase-field elasticity model based on mechanical jump conditions, Comput. Mech. 55 (5) (2015) 887–901.

[51] D. Schneider, F. Schwab, E. Schoof, A. Reiter, C. Herrmann, M. Selzer, T. Böhlke, B. Nestler, On the stress calculation within phase-field approaches: A model for finite deformations, Comput. Mech. 60 (2) (2017) 203–217.

[52] D. Schneider, E. Schoof, O. Tschukin, A. Reiter, C. Herrmann, F. Schwab, M. Selzer, B. Nestler, Small strain multiphase-field model accounting for configurational forces and mechanical jump conditions, Comput. Mech. 61 (3) (2018) 277–295.

[53] S. Sugathan, K. Thekkepat, S. Bandyopadhyay, J. Kim, P.-R. Cha, A phase field model combined with genetic algorithm for polycrystalline hafnium zirconium oxide ferroelectrics, 2022, arXiv preprint arXiv:2204.07960.

[54] I. Steinbach, F. Pezzolla, A generalized field method for multiphase transformations using interface fields, Physica D 134 (4) (1999) 385–393.

[55] J. Zhu, Y. Gao, D. Wang, T.-Y. Zhang, Y. Wang, Taming martensitic transformation via concentration modulation at nanoscale, Acta Mater. 130 (2017) 196–207.

[56] J.-Y. Li, C.-H. Lei, L.-J. Li, Y.-C. Shu, Y.-Y. Liu, Unconventional phase field simulations of transforming materials with evolving microstructures, Acta Mech. Sinica 28 (4) (2012) 915–927.

[57] J.-J. Wang, L.-Q. Chen, Strain control of domain structures in ferroelectric thin films: Applications of phase-field method, in: Handbook of Materials Modeling: Applications: Current and Emerging Materials, Springer, 2020, pp. 1213–1230.

[58] P Hoffrogge, A Mukherjee, ES Nani, PGK. Amos, F Wang, D Schneider, B Nestler, Multiphase-field model for surface diffusion and attachment kinetics in the grand-potential framework, Phys. Rev. E 103 (3) (2021) 033307.

[59] C. Mennerich, F. Wendler, M. Jainta, B. Nestler, A phase-field model for the magnetic shape memory effect, Arch. Mech. 63 (5–6) (2011) 549–571.

[60] C. Mennerich, F. Wendler, M. Jainta, B. Nestler, Rearrangement of martensitic variants in Ni_2MnGa studied with the phase-field method, Eur. Phys. J. B 86 (4) (2013) 1–9.

[61] Y. Sun, C. Beckermann, Sharp interface tracking using the phase-field equation, J. Comput. Phys. 220 (2) (2007) 626–653.

[62] J. Hötzer, A. Reiter, H. Hierl, P. Steinmetz, M. Selzer, B. Nestler, The parallel multi-physics phase-field framework Pace3D, J. Comput. Sci. 26 (2018) 1–12.

[63] J. Hlinka, P. Marton, Phenomenological model of a 90° domain wall in $BaTiO_3$-type ferroelectrics, Phys. Rev. B 74 (10) (2006) 104104.

[64] S.H. Wemple, M. Didomenico Jr., I. Camlibel, Dielectric and optical properties of melt-grown $BaTiO_3$, J. Phys. Chem. Solids 29 (10) (1968) 1797–1803.

[65] L. Li, L. Xie, X. Pan, Real-time studies of ferroelectric domain switching: A review, Rep. Progr. Phys. 82 (12) (2019) 126502.

[66] J.Y. Li, R.C. Rogan, E. Üstündag, K. Bhattacharya, Domain switching in polycrystalline ferroelectric ceramics, Nature Mater. 4 (10) (2005) 776–781.